CDDpress

www.nature.com/cdd

ARTICLE OPEN

Check for updates

Fatty acid channelling into triglycerides and oxylipins drives ferroptosis resistance during oncogenic BRAF-induced senescence

Markus S. Hess[1,2,12], Kamal M. Al-Shami[1,2,12], Carolina Dehesa Caballero[1,2], Julie Haenlin[1,2], Adriano B. Chaves-Filho[1,3], Lisa Schlicker[1,11], Philipp Poeller[1,2], Felix C. E. Vogel[1], Ioanna Koltsaki[1], Deniz Gedik[1], Marta Campos Alonso[1], Susanne Walz[4], Carsten P. Ade[5], Martin Eilers[5], Beate K. Straub[6], Jochen S. Utikal[7,8,9], Svenja Meierjohann[10], Mathias T. Rosenfeldt[10], Marteinn T. Snaebjornsson[1] and Almut Schulze[1]✉

Oncogene-induced senescence (OIS), a cellular programme initiated by activation of oncogenic signalling, provides a barrier to transformation and is accompanied by major reprogramming of cellular metabolism. We show here that induction of OIS by $BRAF^{V600E}$ expression in human diploid fibroblasts led to global changes in the cellular lipidome, characterised by a strong increase in triglycerides (TG) and a marked reduction in membrane phosphoglycerides carrying polyunsaturated fatty acids (PUFA) in their acyl-chains. Induction of $BRAF^{V600E}$ OIS resulted in a marked resistance towards lipid peroxidation and ferroptosis. Inhibition of TG synthesis by blocking diacylglycerol O-acyltransferase 1 (DGAT1) resulted in PUFA re-distribution to membrane lipids and increased ferroptosis sensitivity of senescent cells. Inhibition of DGAT also altered the senescence-associated secretory phenotype (SASP) and enhanced the secretion of oxylipins by $BRAF^{V600E}$ OIS cells. Combined blockade of DGAT1-dependent TG and COX2-dependent oxylipin synthesis fully restored ferroptosis sensitivity in $BRAF^{V600E}$ OIS cells. Together, these findings indicate that channelling of PUFA towards TG synthesis confers protection from oxidative stress and ferroptosis during $BRAF^{V600E}$ OIS but also limits the production of pro-inflammatory lipid mediators, a key feature of the senescent phenotype.

Cell Death & Differentiation; https://doi.org/10.1038/s41418-026-01766-x

INTRODUCTION

Oncogene-induced senescence (OIS) acts as a major barrier to tumourigenesis by inducing a stable growth arrest via activation of TP53, CDKN2A and CDKN1A [1]. In addition, cell-extrinsic events that involve components of the senescence-associated secretory pathway (SASP) induce senescence of neighbouring potentially malignant cells and also facilitate the elimination of cells expressing activated oncogenes through immune surveillance [2]. However, SASP factors have also been linked to pro-tumorigenic processes, including migration, invasion, angiogenesis and immune suppression. For example, it has been shown that OIS-driven SASP promotes tumour formation by inhibiting natural killer (NK) and CD8 T cells [3, 4]. In addition, it is becoming clear that senescent cancer cells enter a stem-like state that is maintained upon cell cycle re-entry, resulting in highly aggressive relapse [5]. Thus, strategies for the effective elimination of senescent cells represent a clinical opportunity.

Senescence is associated with global reprogramming of cellular metabolism [6]. Suppression of nucleotide metabolism by down-regulation of ribonucleotide reductase subunit M2 (RRM2) was shown to be required for the induction and maintenance of OIS triggered by activated RAS, NRAS and BRAF [7]. OIS induced by oncogenic BRAF ($BRAF^{V600E}$), an oncogene frequently mutated in melanoma, was shown to activate pyruvate metabolism via the tricarboxylic acid (TCA) cycle by activating pyruvate dehydrogenase (PDH) [8]. Furthermore, induction of senescence by cytotoxic drugs in lymphoma resulted in elevated glucose and fatty acid metabolism [9]. A similar induction of fatty acid oxidation has also been reported in Ras-induced senescent human fibroblasts [10]. The high metabolic activity of senescent cells, coupled with defects in the respiratory chain, can lead to the production of reactive oxygen species (ROS), resulting in oxidative and proteotoxic stress, further exacerbated by the high protein synthesis demand of the SASP [11]. In addition, mitochondrial

[1]Division of Tumor Metabolism and Microenvironment, German Cancer Research Center (DKFZ), Heidelberg, Germany. [2]Faculty of Biosciences, Heidelberg University, Heidelberg, Germany. [3]Department of Biochemistry, Institute of Chemistry, University of São Paulo, São Paulo, Brazil. [4]Comprehensive Cancer Center Mainfranken, Würzburg, Germany. [5]Biochemistry and Molecular Biology, Theodor-Boveri-Institute, Biocenter, Am Hubland, Würzburg, Germany. [6]Institute of Pathology, University Medical Center of the Johannes Gutenberg University Mainz, Mainz, Germany. [7]Skin Cancer Unit, German Cancer Research Center (DKFZ), Heidelberg, Germany. [8]Department of Dermatology, Venereology and Allergology, University Medical Center Mannheim, Heidelberg University, Mannheim, Germany. [9]DKFZ Hector Cancer Institute at the University Medical Center Mannheim, Heidelberg, Germany. [10]Institute of Pathology, Julius Maximilians University and Comprehensive Cancer Center (CCC) Mainfranken, Würzburg, Germany. [11]Present address: Luxembourg Centre for Systems Biomedicine (LCSB), University of Luxembourg, Belvaux, Luxembourg. [12]These authors contributed equally: Markus S. Hess, Kamal M. Al-Shami. ✉email: Almut.schulze@dkfz-heidelberg.de

Received: 30 September 2025 Revised: 13 April 2026 Accepted: 13 May 2026
Published online: 26 May 2026

dysfunction can itself induce senescence, albeit with a distinct secretome [12].

While reprogramming of glucose and pyruvate metabolism in senescence has been well described, the consequences of senescence on lipid metabolism are less well understood. It has been shown that senescence leads to the production of oxylipins, a class of lipid mediators produced from polyunsaturated fatty acids (PUFA) via enzymatic and non-enzymatic processes [13]. Interestingly, oxylipins produced by senescent cells can function in an autocrine manner to reinforce the senescent state [13]. Oxylipins are synthesised from PUFA that are released from unsaturated membrane lipids by the action of phospholipases [14, 15]. Importantly, the abundance of PUFA also determines the sensitivity of membranes towards lipid peroxidation and ferroptosis, an iron-dependent form of cell death linked to the toxic accumulation of lipid peroxides [16–19]. Altered lipid metabolism could thus impose selective vulnerabilities that may help to eliminate senescent cells.

Here, we show that activation of $BRAF^{V600E}$-induced OIS in human diploid fibroblasts leads to profound lipidome remodelling characterised by the accumulation of large amounts of triglycerides (TG) that are then stored in lipid droplets (LD). Furthermore, we found that OIS cells are protected from lipid peroxidation and ferroptosis induced by multiple ferroptosis inducers (FINs) targeting the GSH/glutathione peroxidase 4 (GPX4) axis or chemical oxidants. Inhibition of TG synthesis by blocking O-diacylglycerol acetyltransferases 1 (DGAT1) selectively impaired the sequestration of PUFA into TG and increased ferroptosis sensitivity in senescent cells. We also found that inhibition of TG synthesis in $BRAF^{V600E}$ OIS cells increased secretion of oxylipins and affected the induction of SASP factors. Finally, combined inhibition of DGAT1 and COX2 resulted in complete restoration of ferroptosis sensitivity of senescent cells. Our results suggest that reprogramming of lipid metabolism contributes to oxidative stress resistance and ferroptosis protection during senescence and also shapes the senescent phenotype.

MATERIAL AND METHODS

Materials

DMEM was obtained from Gibco (21969035). Lipidomics splash mixture (330707) was purchased from Avanti Polar Lipids Inc (Alabaster, AL, USA). 1S,3R-RSL3, ammonium formate, ammonium acetate, DGAT1 inhibitor T863 (SML0539), DGAT2 inhibitor PF-06424439 (PZ0233), etoposide (E1383), celecoxib (SML3031), erastin (E7781), FIN56 (SML1740), cumene hydroperoxide (247502), tert-butyl-hydroperoxide (458139) and ferrostatin (SML0583) were from Sigma-Aldrich (St Louis, MO, USA). $FINO_2$ (HY-129457) was from MedChemExpress.

pRT3-GEPIR-$BRAF^{V600E}$ was generated by amplifying the coding sequence of $BRAF^{V600E}$ from pBabe-puro-$BRAF^{V600E}$ (a gift from R. Marais, Manchester) and inserting it into pRT3-GEPIR (a gift from L. Zender, Tübingen).

Tissue culture and reagents

TIGig3-hTERT cells were obtained from M. Rosenfeldt. IMR90 and WI-38 were obtained from ATCC. BJ-$HRAS^{V12G}$:ER cells were a gift from F. Loayza-Puch (Heidelberg). All primary human diploid fibroblast cell lines were used at low passage. Cells were cultured in Dulbecco's Modified Eagle Medium. DMEM supplemented with 10% foetal calf serum (FCS), 2 mmol/L glutamine and 100 µ/mL penicillin/streptomycin (all Sigma). Cells were grown at 37 °C in a humidified incubator at 3% O_2 (TIG3-hTERT) or 5% CO_2 (all other cell lines) and regularly tested for the absence of mycoplasma.

Retroviral transduction and gene knockout

Retroviral particles were produced by transfection of pRT3-GEPIR-$BRAF^{V600E}$ into Phoenix Eco cells and used to infect TIG3-hTERT cells using 8 µg/mL of polybrene. Cells were selected with 8 µg/mL of blasticidin for 6 days.

For CRISPR/Cas9-mediated deletion of DGAT1, DGAT2 and PTGS2, sgRNA sequences were designed using CHOPCHOP (https://chopchop.cbu.uib.no), VBC-score (https://www.vbc-score.org), or the Broad CRISPick tool (https://portals.broadinstitute.org/gppx/crispick/public). Cloning for knockout was done into lentiCRISPRv2 (Addgene #98291). Viral particles were produced in HEK293T cells and stable populations were selected using the respective agent and used as pools. Knockout efficiency was confirmed using RT-qPCR and functional assays. The following gRNA sequences were used:

DGAT1_KO #7 AGTGGCTTCAGCAACTACCGTGG;
DGAT2_KO #14 AGGTGGCAGGAGGTCACAGTGGG.

Cell lysis and western blotting

Cells were lysed in RIPA buffer (150 mM NaCl, 50 mM Tris pH 8.0, 1% (v/v) NP-40, 0.5% (w/v) sodium deoxycholate, 0.1% (w/v) SDS) with protease and phosphatase inhibitors for 30 min and cleared by centrifugation. Proteins were quantified using BCA (Thermo Scientific). Proteins were separated on SDS-PAGE and blotted onto PVDF membrane (Immobilon), treated with blocking solution (Thermo Scientific) and incubated with primary and secondary antibodies. Signals were detected on a ChemiDoc (BioRad). Antibodies used were: anti-B-Raf (Santa Cruz, sc-5284), anti-COX1 (Cell Signalling, 4841), anti-COX2 (D5H5 XP®) (Cell Signalling, 12282), anti-p16 (Bimake, A5869), anti-p44/42 MAP Kinase (Cell Signalling, 9102), anti-phospho-p44/42 MAP Kinase (Cell Signalling, 9106), anti-Perilipin 2 (Cell Signalling #45535), anti-FASN (BD Transduction Labs, 610962), anti DGAT1 (GeneTex, GTX48577), anti DGAT2 (Proteintech, 17100-1-AP), anti-vinculin (Clone hVIN-1, Sigma, V9131) and anti-actin B (Sigma, A5441). Fluorescent secondary antibodies were from BioRad, HRP-conjugated secondary antibodies were from GE Healthcare (goat anti-mouse, NA931V) and Dako (swine anti-rabbit, P0217).

RNA extraction and RT-qPCR

Total RNA was isolated using peqGOLD TriFast™ (Peqlab), followed by reverse transcription into complementary DNA (cDNA) using M-MLV Reverse Transcriptase (Promega) and random hexamer primers. Real-time qPCR was performed using Power SYBR™ Green PCR Master Mix (Thermo Fisher Scientific) using Quantitect primers (Qiagen) or custom primers (Sigma). Custom primers sequences are the following:

DGAT1 forward 5′-GCTACAGGTCATCTCAGTGCTC-3′,
reverse 5′-TTCTGCCAGTGCCTCTTTGCTG-3′;
DGAT2 forward 5′-GCTACAGGTCATCTCAGTGCTC-3′
reverse 5′-GTGAAGTAGAGCACAGCGATGAG-3′;
IL6 forward 5′-AGACAGCCACTCACCTCTTCAG-3′,
reverse 5′-TTCTGCCAGTGCCTCTTTGCTG-3′ [20];
CDKN2A forward 5′-CCCCTTGCCTGGAAAGATAC-3′,
reverse 5′-AGCCCCTCCTCTTTCTTCCT-3′;
CDKN1A forward 5′-TCACTGTCTTGTACCCTTGTGC-3′,
reverse 5′- CGTTTGGAGTGGTAGAAA-3′;
PLA2G4A forward 5′-GATGAAACTCTAGGGACAGCAAC-3′,
reverse 5′-CTGGGCATGAGCAAACTTCAA-3′ [21];
PTGES forward 5′- GAGGATGCCCTGAGACACGGA-3′,
reverse 5′- CCAGAAAGGAGTGA CGAAGCC-3′;
SCD forward 5′-CCTAGAAGCTGAGAAACTGGTGA-3′,
reverse 5′- ACATCATCAGCAAGCCAGGT-3′;
FADS1: QuantiTect Primer Assay (QT01003800, Qiagen),
FADS2: QuantiTect Primer Assay (QT00077175, Qiagen);
IL1A: QuantiTect Primer Assay (QT00001127, Qiagen);
IL1B: QuantiTect Primer Assay (QT00021385, Qiagen);
RPL13 forward 5′-GAGACAGTTCTGCTGAAGAACTGAA-3′,
reverse 5′-TCCGGACGGGCATGAC-3′ [22].

BrdU labelling

Cells were incubated in 10 µM BrdU-containing media for 30 min, washed with phosphate buffered saline (PBS) and fixed with 80% EtOH. Cells were washed with ice-cold PBS and incubated in HCL/Triton X-100 at room temperature for 30 min. Cells were resuspended in $Na_2B_4O_7$, centrifuged, resuspended in 1% bovine serum albumin (BSA) in PBS/Tween and incubated with anti-BrdU V450 antibody (BD, 560810) at room temperature for 30 min. Cells were washed with 1% BSA in PBS/Tween, and resuspended in $Na_3C_6H_5O_7$. Cells were incubated with RNaseA and PI at 37 °C for 30 min. Samples were analysed using a BD Canto FACs Analyzer and FlowJo software.

Senescence-associated β-galactosidase and heterochromatin formation

For SA β-gal, cells were plated on coverslips followed by fixation with 0.2% glutaraldehyde/2% formaldehyde. SA β-gal activity was assessed as

described [23]. To determine heterochromatin formation, cells were fixed in 4% formaldehyde and stained with Hoechst 33342 (Thermo Fisher Scientific) as described [24]. To quantify, at least 200 cells per coverslip were counted and the percentage of SAHF-positive nuclei was calculated.

Lipidomics and total fatty acid analysis

Cells were washed with cold ammonium acetate (154 mM), scraped off in 0.5 mL ice-cold MeOH/H_2O (80/20, v/v) and snap-frozen in liquid nitrogen. The suspension was transferred to a glass tube and additional 0.5 mL ice-cold MeOH/H_2O (80/20, v/v) was added. The suspensions were cell number adjusted, and internal standards were added (for total fatty acid analysis: 10 µL of 100 µM mix of palmitic acid-D2, oleic acid-D2 and arachidonic acid-D8 (all Eurisotop); for lipidomics: 8 µL of SPLASH® LIPIDOMIX® Standard Mix (Sigma-Aldrich)). Lysates were transferred to glass tubes and extracted following the Bligh & Dyer protocol [25]. Organic phases were transferred to new glass tubes, dried under gas nitrogen and resuspended in 200 µL isopropanol. For saponification of total fatty acids, 50 µL of the extract was resuspended in 2 mL 0.3 M KOH in MeOH/H_2O (9/1, v/v), mixed vigorously and incubated at 80 °C for 1 h. Samples were washed twice using 2 mL n-hexane. 200 µL formic acid was added to the lower phase and fatty acids were extracted twice with 2 mL n-hexane. Upper phases were collected, combined and taken to dryness under a stream of nitrogen at 45 °C. Resulting residues were dissolved in 100 µL isopropanol and taken for LC-MS analysis using a Q Exactive Plus (Thermo) interfaced with a Vanquish ultra-high-performance liquid chromatography (Thermo).

Targeted lipidomics and fatty acid analysis. Lipid and total fatty acid extracts (3 µL) were loaded onto an Accucore® C8 column (2.6 µm particle size, 50 × 2.1 mm, Thermo Scientific). Mobile phase buffer A consisted of CH_3CN/H_2O/FA (10/89.9/0.1, v/v/v) and mobile phase buffer B consisted of CH_3CN/iPrOH/H_2O/FA (45/45/9.9/0.1, v/v/v/v). After sample application at 40 °C, the LC gradient programme for lipids was 20% solvent B for 2 min, followed by a linear increase to 99.5% solvent B within 5 min, then maintaining 99.5% solvent B for 27 min, then returning to 20% solvent B within 1 min. For fatty acids, the LC gradient programme was 20% solvent B for 1 min, followed by a linear increase to 99% solvent B within 15 min, then maintaining 99% solvent B for 13 min, then returning to 20% solvent B within 1 min. The column was equilibrated at 20% solvent B for 5 min prior to every injection. The flow rate was maintained at 350 µL/min. The eluent was directed to the ESI source of the MS instrument for lipids from 2.0 min to 35 min and for fatty acids from 3.0 min to 27 min after sample injection. MS analysis was performed on a Q Exactive Plus mass spectrometer (Thermo Scientific). For detection of lipids, the following scan and HESI source parameters were applied in positive and negative mode: 200–1600 *m/z*; resolution: 70,000; AGC-Target: 1E6 counts; maximum injection time: 50 ms; sheath gas: 30 au; auxiliary gas: 5 au; aux gas heater temperature: 120 °C; spray voltage: 2.5 kV; capillary temperature: 320 °C; S-lens RF level: 55.0%. For fragmentation of lipids, the following ddMS2 settings were applied in positive and negative mode: Resolution: 17,500; AGC-Target: 1E5 counts; maximum injection time: 50 ms. For detection of fatty acids, the following scan and HESI source parameters were applied in negative mode: 20–380 *m/z*; resolution: 70,000; AGC-Target: 1E6 counts; maximum injection time: 50 ms; sheath gas: 30 au; auxiliary gas: 10 au; aux gas heater temperature: 120 °C; spray voltage: 2.5 kV; capillary temperature: 320 °C; S-lens RF level: 55.0%. Signal determination and quantitation were performed using El-Maven Version 0.12.0 (Elucidata Inc).

Non-targeted lipidomics. Lipid extracts (2 µL) were loaded onto a BEH® (UPLC® C18 column, 1.7 µm, 2.1 mm i.d. × 100 mm) with a flow rate of 0.2 mL min−1 and the oven temperature was maintained at 45 °C. For reverse-phase LC, mobile phase A consisted of water/acetonitrile (60:40), and mobile phase B was composed of isopropanol/acetonitrile/water (88:10:2). Mobile phases A and B contained 5 mM ammonium formate and 0.1% formic acid. Lipids were separated by a 20 min linear gradient as follows: from 40 to 100% B for the first 10 min, then held at 100% B from 10 to 12 min, decreased from 100 to 40% B during 12–13 min, and held at 40% B from 13 to 20 min. The MS was operated in both positive and negative ionization modes, and the scan range was set at a mass-to-charge ratio of 350-1300 Da and 350–1600 Da, respectively. The mass spectrometry was operated using sheath gas flow rate: 30; auxiliary gas flow rate: 10; sweep gas flow rate: 0; spray voltage: 3.6 kV (positive)/2.5 kV (negative); capillary temperature: 320 °C; S-lens RF level: 55.0; auxiliary gas heater temperature: 120 °C. Data acquisition on MS was performed using the following settings: mass resolution = 70,000 at *m/z* 200, Automatic Gain Control (AGC) = 1×10^6, and Injection Time (IT) = 50 ms. Data for lipid molecular species identification and quantification was obtained by data-dependent acquisition using the following settings: mass resolution = 17,500 at *m/z* 200, AGC = 1×10^5; IT = 50 ms; isolation window = 1.2 *m/z*; collision energy (CE) = 20/40/60; dynamic exclusion = 10 s; and Minimum AGC target to trigger MS/MS = 2×10^3. Lipid molecular species were manually identified based on their specific fragments and/or neutral losses, retention time and exact *m/z*. Data was analyzed with the help of SeeMS software. After identification, the peak area of each lipid specie was obtained using El-Maven. The area ratio obtained for each lipid was normalized by the peak area of its corresponding internal standard. The concentration of lipid molecular species and fatty acids was estimated by multiplying the area ratio by the concentration of the corresponding internal standard.

Lipid droplet detection

Cells were grown on glass cover slips, washed with PBS and fixed with 3.7% PFA for 10 min. Cells were stained with 0.1 µg/ml LD540 for 30 min, washed three times with PBS and once in water. Nuclei were stained in a 30 nM DAPI solution (Invitrogen, D1306) in PBS for 5 min, washed and mounted with mounting medium (ThermoFisher Scientific, P36961). Cells were analysed by confocal microscopy (Leica TCS SP8).

Histological analysis

Archived tissue from human melanocytic naevi was obtained from University Medical Center Mannheim with informed consent. The study was conducted in accordance with the principles of the Declaration of Helsinki and approved by the Ethics Committee II of Heidelberg University (2010-318N-MA and 2014-835R-MA). Double-label immunohistochemistry was performed on formalin-fixed, paraffin-embedded tissues cut at a size of max. 5 µm. After antigen retrieval, tissue slides were stained sequentially with the respective mouse monoclonal antibodies against p16 (Agilent, clone J9, ready to use, ref. nr. GA78361-2) and perilipin 2 (Progen Biotechnics, AP125, ready to use, catalog-nr. 610102). Staining was done using an automated staining system (DAKO Autostainer plus, Agilent Technologies, Santa Clara, CA, USA) and the Dako EnVision FLEX staining system (Agilent Technologies, Santa Clara, CA, USA) in accordance with the manufacturer's instructions.

RNAseq and data analysis

RNA was extracted using RNeasy columns (Qiagen), including DNase I digestion. mRNA was isolated using NEBNext® Poly(A) mRNA Magnetic Isolation Module and library preparation was performed with NEBNext® Ultra™ RNA Library Prep Kit for Illumina following the manufacturer's instructions. Libraries were size-selected using Agencourt AMPure XP Beads (Beckman Coulter) followed by amplification with 12 PCR cycles. Library quantification and size determination were performed with an Experion system (Bio-Rad), and libraries were sequenced with NextSeq500 (Illumina) at the Bioinformatics Core Unit of the Comprehensive Cancer Center Mainfranken. Reads were aligned to the human genome (hg19) with TopHat2, Bowtie v0.12.8, using default parameters. Mapped reads per gene (EnsEMBL GRCh37, release 74) were counted using the "summarizeOverlaps" function in the GenomicAlignments R package, non-expressed genes were removed (mean read count per gene over all samples >1), and TMM normalized with EdgeR. Gene set enrichment analyses were performed using MSigDB v5.2 with default parameters and 1000 permutations. RNAseq data have been uploaded to Gene Expression Omnibus and will be made available upon publication (GSE326013).

Detection of relative cell number using crystal violet staining and automated cell counting

Cells were washed with PBS and fixed for 10 min in 3.7% paraformaldehyde (PFA). Cells were washed again and stained with 0.1% crystal violet solution for 30 min. Plates were rinsed in water, dried and extracted using 10% acetic acid. Absorbance was measured at 585 nm.

Automated cell counting was conducted using the IncuCyte® S3 Live-Cell Analysis System (Sartorius). Brightfield images were captured using the IncuCyte system sitting in a humidified incubator at 37 °C and 5% CO_2. Quantification of live and dead cells was performed using the integrated IncuCyte AI Cell Health Analysis Software Module and subsequent Cell-by-

Cell-analysis of the Cytotox Dye (Sartorius 4633) according to manufacturer's instructions.

Stable isotope labelling

Cells were incubated in DMEM medium without glucose supplemented with 25 mM [U-^{13}C]-glucose (Cambridge Isotope Laboratories) for 24 h. Cells were washed with ice-cold ammonium acetate (154 mM), snap-frozen in liquid nitrogen, and scraped off in 500 µL MeOH/CH_3CN/H_2O (50/30/20, v/v/v) containing 4 µM of the internal standards glutaric acid-D4 and phenylalanine-D8. RP18 SPE-columns were activated by elution of 1 mL CH_3CN and equilibrated by elution of 1 mL MeOH/CH_3CN/H_2O (50/30/20, v/v/v). Cleared cell extracts were loaded onto RP18 SPE-columns, and eluates were collected in new tubes. Remaining cell pellets were resuspended in 0.5 mL ice-cold MeOH/CH_3CN/H_2O (50/30/20, v/v/v), mixed, sonicated and cleared by centrifugation. Supernatants were transferred to the same column again, and eluates were collected in the same tubes as before. Eluates were taken to dryness in a vacuum concentrator and analysed as described below. Extracts (3 µL) were applied to an Accucore Amide-HILIC column (2.6 µm particle size, 100 × 2.1 mm, Thermo Scientific). Mobile phase buffer A consisted of 5 mM ammonium acetate in 5% acetonitrile and mobile phase buffer B consisted of 5 mM ammonium acetate in 95% CH3CN. After sample application at 30 °C, the LC gradient programme was 98% solvent B for 1 min, followed by a linear decrease to 40% solvent B within 5 min, then maintaining 40% solvent B for 13 min, then returning to 98% solvent B within 1 min. The column was equilibrated at 98% solvent B for 5 min prior every injection. The flow rate was maintained at 350 µL/min. The eluent was directed to the electrospray ionization (ESI) source of the MS instrument from 0.5 to 19 min after sample injection. MS analysis was performed on a Q Exactive Plus mass spectrometer (Thermo Scientific). For the detection of water-soluble metabolites, the following scan and heated electrospray ionization (HESI) source parameters were applied in positive and negative mode: 69–1000 *m/z*; resolution: 70,000; AGC-Target: 1E6 counts; maximum injection time: 50 ms; sheath gas: 30 au; auxiliary gas: 10 au; aux gas heater temperature: 120 °C; spray voltage: 3.6 kV (pos)/2.5 kV (neg); capillary temperature: 320 °C; S-lens RF level: 55.0%. For the fragmentation of water-soluble metabolites, the following ddMS2 settings were applied in both modes: Resolution: 17,500; AGC-Target: 1E5 counts; maximum injection time: 50 ms; Loop count: 1; CE: 20, 50, 80 eV; Apex trigger: 0.1 to 10 s; minimum AGC target: 2E3 counts; Dynamic exclusion: 20 s.

Lipid peroxidation analysis

To determine lipid peroxidation by FACS, cells were treated with RSL3 and/or ferrostatin-1 as indicated, washed twice with HBSS (Gibco #14025-092) and stained with 1 µM Liperfluo (Dojindo) in HBSS for 30 min. Cells were dissociated using Accutase (Sigma-Aldrich) for 5 min, washed and stained with 30 nM DAPI for 10 min. Cells were analysed by flow cytometry on a FACS-Calibur Flow Cytometer (BD Biosciences).

To assess lipid peroxidation in live cells using the C11-BODIPY$^{581/591}$ sensor (Thermo Fisher Scientific #D3861), cells were seeded in a 24-well format and treated as indicated. After washing with prewarmed HBSS$^{+/+}$, cells were incubated with 5 µM C11-BODIPY$^{581/591}$ in HBSS$^{+/+}$ at 37°C for 20 min. Cells were washed again with HBSS$^{+/+}$ and treated with RSL3 and/or ferrostatin-1 in DMEM containing 10% FBS. Cells were imaged with brightfield, red (Ex. 567–607 nm, Em. 622–704 nm) and green (Ex. 441–481 nm, Em. 503–544 nm) fluorescence channels using an IncuCyte S3 system. Image analysis was conducted using the AI Cell Health Analysis Software Module and subsequent Cell-By-Cell Analysis Software Module.

Transmission electron microscopy (TEM)

TIG3-BRAF^{V600E} cells were treated as indicated, seeded on glass coverslips and fixed in 2% formaldehyde, 2% glutaraldehyde, 1 mM $CaCl_2$, 1 mM $MgCl_2$, and 100 mM cacodylate buffer (pH 7.2). After three washes in 40 mM cacodylate buffer, cells were postfixed in 2% osmium tetroxide in 40 mM cacodylate for 30 min on ice in the dark. Samples were rinsed in distilled water and dehydrated by sequential dipping into 30% and 50% ethanol (total 30 min), followed by 1% uranyl acetate in 75% ethanol for 30 min and final dehydration in 100% ethanol (three changes, 30 min total). Specimens were infiltrated with ethanol/Epon (3:1) for 20 min, transferred through propylene oxide/Epon (1:1), and placed in neat Epon overnight at room temperature. Coverslips were flat-embedded in fresh Epon (12 g glycidyl ether, 6.5 g DDSA, 6.5 g NMA, 400 µl DMP-30) and polymerized at 60 °C for 3 days. Ultrathin sections were cut at 50 nm nominal thickness using a Leica Ultracut UCT (Leica, Wetzlar, Germany) and examined by transmission electron microscopy to assess cellular structures. Images were acquired using a Zeiss EM 910 (Carl Zeiss, Oberkochen, Germany) transmission electron microscope operated at 80 kV and equipped with a 2k slow-scan CCD Camera (TRS, Moorenweis, Germany).

Oxylipin analysis

Cells were washed, and medium was replaced with phenol red free DMEM and incubated for 24 h. Briefly, 500 µL of media or PBS (extraction blank) was added to 100 µL of internal standard mixture containing 250 ng/mL 13(S)-HODE-d_4, (±)12(13)-DiHOME-d_4 and PGE_2-d_4. Oxylipins were extracted by solid phase extraction (SPE) using Strata C18-E columns (50 mg; 8B-S001-DAM, Phenomenex). SPE columns were washed with 2 mL of MeOH and equilibrated with 2 mL of ultrapure water before loading samples. Then, SPE columns were washed with 1 mL of 5% MeOH and oxylipins were eluted with 1 mL 100% MeOH. The eluate was dried under a stream of nitrogen gas, dissolved in 50 µL MeOH and immediately analysed by LC-MS/MS. Oxylipin analysis was carried out on the same LC-MS instrument described above. Samples (5 µL) were loaded into a BEH® (UPLC® C18 column, 1.7 µm, 2.1 mm i. d. X 100 mm, Waters) with a flow rate of 0.4 mL min^{-1} and the oven temperature maintained at 40 °C. For reverse-phase LC, the mobile phase A consisted of CH_3CN/H_2O/Formic acid (30/70/0.02, v/v/v) and mobile phase B consisted of CH_3CN/iPrOH (70/30, v/v). Oxylipins were separated by a gradient as previously described [26]. For detection of oxylipins, the following ion source parameters were applied in negative ionisation mode: sheath gas: 30 au; auxiliary gas: 10 au; aux gas heater temperature: 120 °C; spray voltage: 2.5 kV (neg); ion transfer temperature: 320 °C; S-lens RF level: 55.0%. Data acquisition was performed by parallel reaction monitoring (PRM) analysis. PRM data were acquired with following settings: resolution: 17,500 at 200 *m/z*; AGC-Target: 5E4 counts; maximum injection time: 50 ms; isolation window: 1.5 *m/z*. Detailed information about the oxylipins monitored is described in Table S4. Peak area integration of specific fragments for each analyte was performed with Skyline software. For quantification, the area ratio obtained by dividing the peak area of each oxylipin by the corresponding internal standard was applied in a calibrate curve constructed for each analyte.

Statistical analysis

Statistical analyses of data obtained from lipid analyses were performed with Metaboanalyst (www.metaboanalyst.ca). All other statistical analyses were carried out with GraphPad Prism 11. Number of biologically independent replicates for in vitro experiments was chosen based on trial experiments. No samples were excluded. Groups were compared by multivariate (PCA) and/or univariate analyses (*t*-test or ANOVA, $p < 0.05$, FDR-applied) followed by post-hoc tests (Tukey or Sidak's). All data are presented as average ± SD.

RESULTS

Oncogene induced senescence induces triglyceride accumulation and LD formation

OIS is a major barrier to transformation and has previously been linked to reprogramming of glucose and lipid metabolism [8, 10, 27]. To obtain comprehensive insight into the metabolic phenotype of cells undergoing OIS, we established a doxycycline-inducible expression system of oncogenic BRAF (BRAF^{V600E}) in TIG3 human diploid fibroblasts (Fig. 1a). Induction of BRAF^{V600E} expression resulted in time-dependent activation of ERK1/2 phosphorylation, increased expression of p16 protein and resulted in a stable reduction in S-phase (Figs. 1b and S1a, b). We also detected senescence-associated β-galactosidase (SA-β-gal) activity and senescence-associated heterochromatin formation (SAHF) to confirm the senescent state (Figs. 1c, d and S1c, d). Moreover, genes linked to senescence and the senescence-associated secretory phenotype (SASP), namely interleukin 1 beta (*IL1B*), interleukin 1 alpha (*IL1A*), interleukin 6 (*IL6*) and p16 (*CDKN2A*), were strongly induced (Fig. 1e, f).

To reveal how the profound functional alterations induced by senescence affect cellular lipid metabolism, we conducted targeted lipidomic analysis using liquid chromatography-coupled mass spectrometry (LC-MS) of extracts from cells harvested after different times of BRAF^{V600E} activation, detecting a total of 232

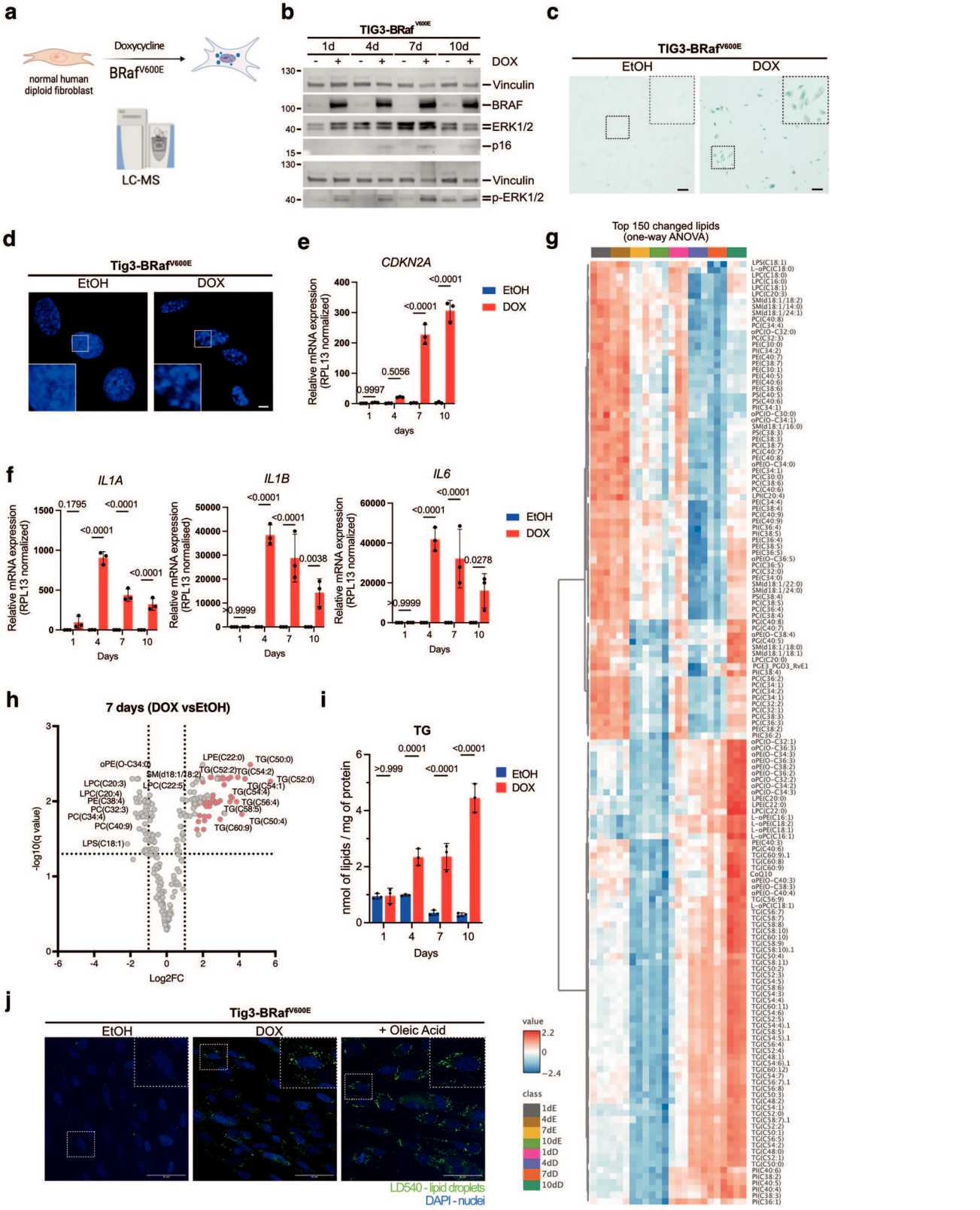

lipid species (Table S1). This revealed major changes in the abundance of lipids from several classes, including a marked reduction of phosphatidylcholine (PC) and phosphatidylethanolamine (PE), the two most abundant membrane lipids, during the early stages of senescence induction. In contrast, levels of phosphatidylinositol (PI), phosphatidylglycerol (PG), O-linked lyso-phosphatidylethanolamine (L-oPE) and O-linked lyso-phosphatidylcholine (L-oPC) were increased in OIS cells (Fig. S1e). The most prominent change was a strong accumulation of triglycerides (TG), observed from day 4 of $BRAF^{V600E}$ activation onwards (Fig. 1g–i).

Fig. 1 Oncogene induced senescence induces reprogramming of lipid metabolism and lipid droplet formation. a Model for the induction of OIS in TIG3 human diploid fibroblasts following $BRAF^{V600E}$ expression. **b** Lysates from TIG3-$BRAF^{V600E}$ fibroblasts treated with 1 μg/ml doxycycline (DOX) or ethanol(solvent, EtOH) for 1, 4, 7 or 10 days were analysed for expression of BRaf and p16 as well as for activation of ERK1/2. Vinculin is shown as loading control. **c** Representative brightfield microscopy image of SA-β-gal staining of TIG3-$BRAF^{V600E}$ cells cultured with 1 μg/ml DOX or EtOH (solvent) for 7 days. Scale bar = 50 μm. **d** Representative fluorescent images of TIG3-$BRAF^{V600E}$ cells cultured with EtOH (solvent) or 1 μg/mL DOX for 7 days and stained with Hoechst. Scale bar = 5 μm. **e**, **f** Expression of *CDKN2A* and the SASP factors *IL1A*, *IL-1B* and *IL6* after 1, 4, 7 and 10 days of $BRAF^{V600E}$ expression in TIG3 cells. Data represent mean ± SD ($n = 3$, significance was calculated using two-way ANOVA with post hoc Sidak's test). **g** Heatmap of intracellular lipidomes of TIG3-$BRAF^{V600E}$ cells treated with 1 μg/ml DOX or EtOH (solvent) for 1, 4, 7 or 10 days. Lipids were analysed by LC-MS ($n = 3$). **h** Volcano plot showing comparison of lipid abundance between DOX and EtOH treated cells at day 7. **i** Abundance of triglycerides (TG) in TIG3-$BRAF^{V600E}$ cells treated with 1 μg/ml DOX or EtOH (solvent) for 1, 4, 7 or 10 days. Data are presented as mean ± SD ($n = 3$; Significance was calculated using one-way ANOVA with post hoc Tukey's test). **j** Lipid droplet staining of TIG3-$BRAF^{V600E}$ cells treated with 1 μg/ml DOX or EtOH (solvent) for 7 days. Cells treated with 50 μM oleic acid are shown as positive control.

TG are stored in lipids droplets (LD), specialised organelles consisting of a phospholipid monolayer and a core of neutral lipids [28]. When we stained TIG3 cells after 7 days of $BRAF^{V600E}$ expression with the neutral lipid dye LD540 [29], cells showed an increased LD abundance, indicating that $BRAF^{V600E}$-induced OIS leads to enhanced synthesis and storage of neutral lipids (Fig. 1j).

Senescence leads to induction of DGAT and PLIN2 and rewiring of glucose metabolism

To elucidate the mechanism underlying the elevated LD presence in senescence, we conducted time-resolved analysis of transcriptional programs induced during OIS progression using RNA-sequencing (Table S2). Gene set enrichment analysis revealed strong and persistent repression of proliferation, while gene sets associated with inflammation showed a peak of induction after 4 days of OIS induction (Fig. S2a). Gene Ontology clustering performed on day 7 revealed downregulation of a gene set cluster linked to cell cycle, chromatin remodelling and cytoskeleton, while clusters linked to cytokine production, secretory processes and hormone metabolism were induced (Fig. S2b). In addition, we observed upregulation of a gene set cluster mapping to the regulation of lipid metabolism, with representative gene sets from this cluster mirroring this induction (Fig. S2c, d). One of these gene sets was also found to be induced following expression of $BRAF^{V600E}$ in single-cell RNAseq data from primary human melanocytes undergoing a stepwise-edited in vitro transformation model (Fig. S2e) [30]. These results indicate that altered lipid metabolism is part of the transcriptional landscape of $BRAF^{V600E}$ OIS cells.

In an orthogonal approach, we conducted a combined pathway analysis focusing on metabolic processes to integrate RNAseq data with metabolomics data derived from cells treated in parallel using MetaboAnalyst (https://www.metaboanalyst.ca/). This showed that glycerolipid metabolism was strongly enriched after 4 days of doxycycline treatment (Fig. 2a). The leading gene in this pathway was diacylglycerol O-acyltransferase 2 (DGAT2), which was strongly induced in response to $BRAF^{V600E}$ activation (Fig. 2b, c). This was not surprising, as *DGAT2* expression is controlled by the X-box binding protein 1 (XBP1) as part of the unfolded protein response [31], which is also activated during OIS [32]. Indeed, we observed strong induction of the XBP1 target DNA damage inducible transcript 3 (*DDIT3*) in response to $BRAF^{V600E}$ activation (Fig. 2c). Furthermore, treatment of OIS cells with the chemical chaperone 4-phenylbutyric acid (4-PBA) reduced expression of *DGAT2* (Fig. S2f).

When analysing protein levels, we confirmed the strong upregulation of DGAT2 observed on RNA levels and revealed a moderate induction of DGAT1 in $BRAF^{V600E}$ OIS cells (Fig. 2d), suggesting that the enhanced production of TG lipids could be mediated by elevated expression of these two enzymes.

As we also observed increased LD abundance, we also interrogated the RNAseq data for expression of perilipin 2 (PLIN2), a major protein linked to lipid droplet formation. This showed that *PLIN2* mRNA was strongly induced from day 4 of $BRAF^{V600E}$ activation onwards (Fig. 2c). Furthermore, PLIN2 protein was also strongly upregulated in OIS cells (Fig. 2e). The link between senescence and increased LD abundance was further demonstrated by histological analysis of human melanocytic naevi. Co-staining of human tissue samples for p16 and PLIN2 revealed the presence of LD in p16-positive areas in 13 of the 19 samples analysed (Figs. 2f and S2g, h), confirming that LD are a common feature of these structures.

Glycerolipids are defined by their three-carbon backbone to which fatty acids are esterified. This moiety is derived from glycerol-3-phosphate, which can be synthesised from glycerol or dihydroxyacetone phosphate (DHAP) generated by glycolysis. As we observed strong but transient induction of glycerol kinase (*GK*) during $BRAF^{V600E}$ mediated OIS (Fig. 2c), we next employed stable isotope tracing with [U-^{13}C]-glucose to interrogate the rewiring of glucose metabolism in OIS cells. In agreement with previous findings [8]. $BRAF^{V600E}$ OIS cells showed an increase in the M + 2 fraction of the TCA cycle metabolites citrate and aconitate (Fig. S3a). Furthermore, we observed that the M + 3/M + 2 ratio of malate was also increased, suggesting TCA cycle anaplerosis from pyruvate and altered NAD metabolism [33] (Fig. S3b). We also observed a strong elevation of ^{13}C-labelled glycolytic intermediates, most notably fructose-1,6 bisphosphate (FBP) and glyceraldehyde-3-phosphate (GAP)/DHAP (Fig. 2g). In agreement with a recent study [34], glycerol-3-phosphate levels were also elevated. In addition, the high abundance of the M + 3 isotopologue of glycerol-3-phosphate indicates a major contribution of glycolysis-derived carbons to the production of this metabolite in OIS cells (Fig. 2g).

Together, these results suggest that enhanced TG synthesis and LD formation in $BRAF^{V600E}$ OIS cells is mediated by changes in the expression of the relevant enzymes and structural proteins combined with the rewiring of glucose metabolism to provide essential metabolic intermediates (Fig. 2h). As fatty acid synthase, the enzyme responsible for fatty acid synthesis, was not induced (Fig. S3c, d), we conclude that fatty acids used for TG synthesis in OIS cells are mostly derived from uptake rather than de novo synthesis.

OIS induced lipidome changes protect cells from ferroptosis

The observed accumulation of TG in OIS cells raised the possibility that reprogramming of lipid metabolism towards lipid storage could affect fatty acid composition of structural lipids that make up biological membranes. Indeed, several membrane lipids carrying fatty acid tails with four or more double bonds, such as PC(34:4) or PE(38:4), were among the strongly downregulated lipids in $BRAF^{V600E}$ OIS cells (see Fig. 1h). We therefore inspected the overall saturation of PC, PE and o-PE lipids and found that lipids with four or more double bonds were generally downregulated, particularly during the early stages of OIS (Fig. 3a). The most abundant PUFA-containing lipids from each class, namely PC(38:5), PE(38:4) and oPE(O-C38:7), were also

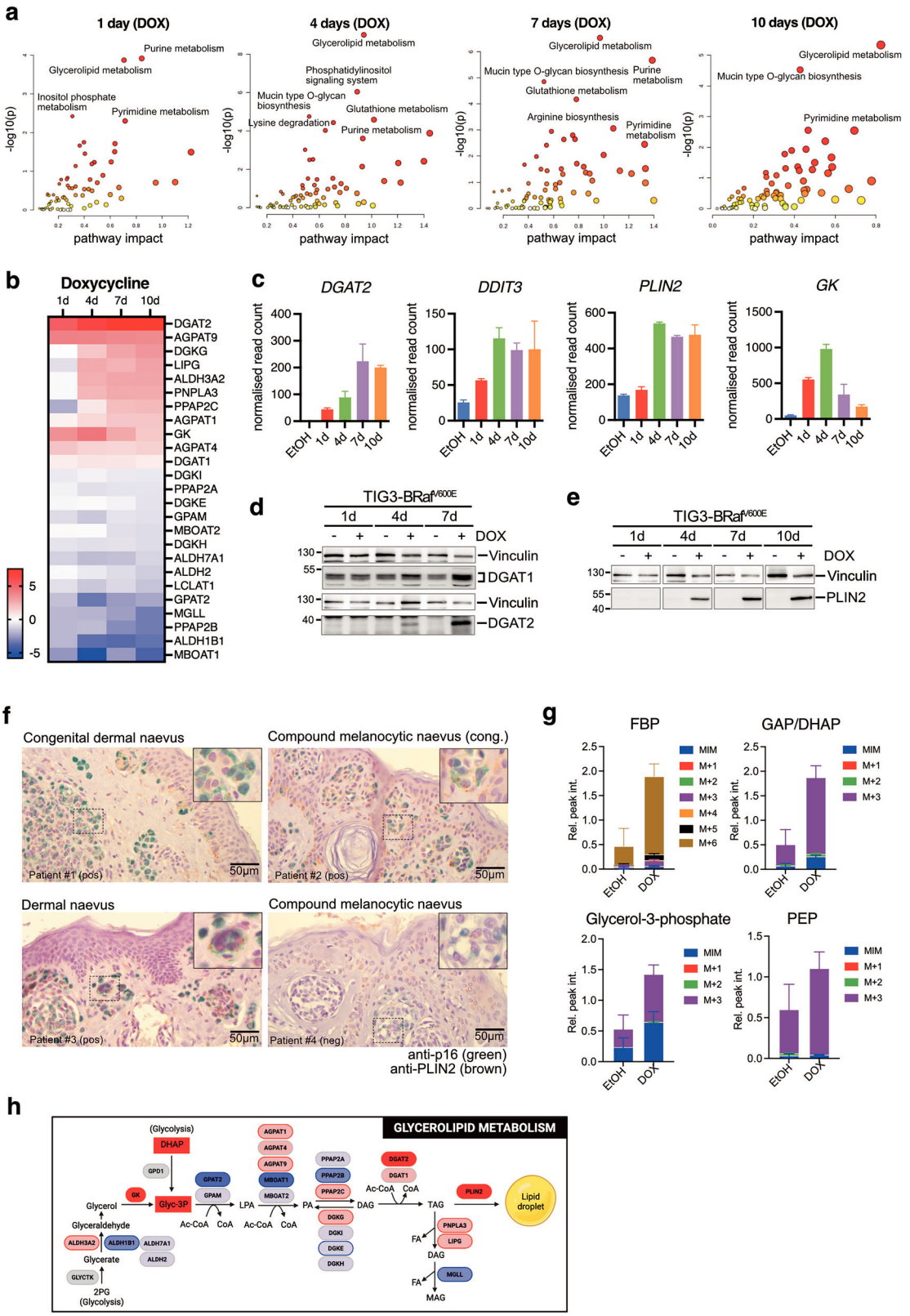

downregulated after 4 and 7 days of BRAF^{V600E} induction (Fig. 3b). While the relative amounts of unsaturated lipids were still decreased, we also noticed that the absolute amounts of some highly unsaturated lipids, particularly oPE with four or more double bonds, were increased after 10 days of BRAF^{V600E} induction (Fig. S4a), mostly reflecting an overall increase of lipids in this class (Fig. S1e). A similar increase in the relative abundance of species with 0-3 double bonds, containing saturated (SFA) and mono-unsaturated fatty acids (MUFA), was also observed in the TG pool

Fig. 2 TG accumulation in OIS is mediated by changes in gene expression and altered glucose metabolism. a Combined pathway analysis integrating RNAseq data from TIG3-BRAF^{V600E} cells treated with 1 μg/ml doxycycline (DOX) for 1, 4, 7 or 10 days compared to 10 days EtOH (solvent) ($n = 2$ independent replicates) and metabolomics data from cells treated in parallel ($n = 3$ independent replicates). **b** Heatmap displaying changes in expression of genes related to glycerolipid metabolism during OIS induction in TIG3-BRAF^{V600E} cells. Data represent log2-fold change relative to solvent control ($n = 2$). **c** Normalised read count for *DGAT2*, *DDIT3*, *PLIN2* and *GK* derived from the same experiment as in **b**. **d** Western blot analysis of lysates from TIG3-BRAF^{V600E} cells treated with 1 μg/ml DOX or EtOH (solvent) for 1, 4, or 7 days for expression of DGAT1 and DGAT2. Vinculin is shown as loading control. **e** Western blot analysis of lysates from TIG3-BRAF^{V600E} cells treated with 1 μg/ml DOX or EtOH (solvent) for 1, 4, 7 or 10 days for expression of PLIN2. Vinculin is shown as loading control. **f** Representative images showing histological sections of human melanocytic naevi stained with antibodies detecting p16 (green) and PLIN2 (brown). **g** TIG3-BRAF^{V600E} cells were treated with 1 μg/ml DOX or EtOH (solvent) for 7 days and subsequently cultured in medium containing 20 mM U-^{13}C-glucose for 24 h. Relative abundance and isotopologue distribution of selected metabolites were analysed using LC-MS. Data are presented as mean ± SD of 3 independent replicates. **h** Diagram indicating metabolic pathway of TG synthesis. Colours indicate increased (red) or decreased (blue) expression/abundance in OIS cells.

(Fig. 3c), suggesting that OIS increases the abundance of these fatty acids in the entire lipidome.

As lipids containing PUFA are highly susceptible to peroxidation and increase the sensitivity of cells towards ferroptosis [35], we next investigated whether BRAF^{V600E} OIS cells display differences in their response to the glutathione peroxidase 4 (GPX4) inhibitor 1S,3R-RSL3 (RSL3). Control cells showed a strong loss of viability in the presence of RSL3, which was accompanied by the appearance of morphological changes characteristic of ferroptosis (Fig. 3d, e). Activation of BRAF^{V600E} for 7 days rendered the cells highly resistant to RSL3 treatment, with no induction of ferroptosis being detected even at the higher doses (Fig. 3d, e).

Dose response treatments revealed a marked difference in IC50 between control and OIS cells (0.25 μM vs 2.3 μM) and ferroptosis as the mode of cell death was confirmed by ferrostatin rescue (Fig. 3f). Moreover, both Liperfluo and Bodipy$^{581/591}$ staining indicated reduced lipid peroxidation after RSL3 treatment in BRAF^{V600E} OIS cells compared to controls (Fig. 3g, h). Using high-throughput live cell imaging, we confirmed that BRAF^{V600E} OIS cells showed resistance to ferroptosis inducers (FINs) from several classes, including the class I FIN erastin, the class II FIN RSL3 and the class III molecule FIN56 (Fig. 3i). Surprisingly, we did not observe protection from the iron oxidant FINO2, a prototype of a class IV FIN (Fig. S4b), suggesting that BRAF^{V600E}-OIS cells are not protected from iron-mediated lipid peroxidation [36]. This is particularly interesting, as iron-mediated lipid peroxidation is initiated in the lysosome [37]. Recent findings have linked lysosomal dysfunction to ferroptosis resistance in replicative and irradiation-induced senescence [38], suggesting that different senescence states may induce specific mechanisms of ferroptosis-resistance.

Nevertheless, senescent TIG3-BRAF^{V600E} cells were also resistant to the direct oxidants tert-butyl hydroperoxide and cumene hydroperoxide (Fig. S4c). Furthermore, modulation of ferroptosis did not per se alter the senescent phenotype, as treatment with ferrostatin did not affect on the induction of *CDKN1A* in BRAF^{V600E} OIS TIG3 cells (Fig. 3j). Ferroptosis protection in response to OIS induced by BRAF^{V600E} was not limited to TIG3 cells, as expression of BRAF^{V600E} in IMR90 or WI-38 human diploid fibroblasts also induced resistance to RSL3. Strong induction of LD formation in senescent WI-38 cells further suggested that deregulation of lipid metabolism is linked to ferroptosis protection across multiple experimental systems (Fig. S4d–f).

We next questioned whether other forms of senescence also lead to protection from ferroptosis. First, we induced IMR90 and WI-38 cells to enter premature senescence by treatment with etoposide for 8 or 6 days, respectively [39, 40]. This caused a marked reduction in sensitivity towards RSL3 treatment in both cell lines, with WI-38 cells also displaying marked accumulation of TG and cholesteryl-esters upon senescence induction (Fig. 3k–m).

We next investigated ferroptosis in the context of OIS induced by activation of oncogenic HRAS. Human BJ fibroblasts expressing an inducible version of HRAS^{G12V} (BJ-HRAS^{V12G}:ER) were induced to undergo OIS by treatment with tamoxifen for 12 days. This caused a strong induction of SA-β-gal and senescence markers (Fig. S4g, h). However, in contrast to BRAF^{V600E} OIS, HRAS^{G12V}-induced OIS cells showed a marked increase in ferroptosis sensitivity (Fig. S4i). Similar results were also observed for TIG3 fibroblasts after induction of HRAS^{G12V} for 7 or 14 days (Fig. S4j). This was not surprising, as ferroptosis has been initially identified as a selective vulnerability of human fibroblasts transformed by HRAS^{G12V} due to increased intracellular iron levels [41, 42].

While our results demonstrate that senescence can be linked to reduced sensitivity towards lipid peroxidation and ferroptosis, they also suggest that different senescence programs shape ferroptosis sensitivity via distinct mechanisms.

Ferroptosis protection in OIS cells is mediated by TG accumulation

Enhanced TG synthesis has already been linked to ferroptosis resistance during cell cycle arrest [43] and in the presence of environmental PUFA [44]. The synthesis of TG requires the activity of DGAT1 or DGAT2, two membrane-bound enzymes with limited structural similarity but overlapping tissue-specific expression patterns [45].

As both DGAT1 and DGAT2 were induced during BRAF^{V600E} OIS, we first investigated the effect of combined inhibition of DGAT1 and DGAT2 on LD formation and lipidome of OIS and control cells. Treatment of cells with inhibitors of DGAT1 and DGAT2 completely abolished LD formation in senescent cells (Fig. 4a). Furthermore, while DGAT inhibition only had a minor effect in control cells but resulted in the strong downregulation of TG in OIS cells without altering the total abundance of other lipid classes (Figs. 4b and S5a, and Table S3). We next determined the effect of DGAT inhibition on fatty acid composition of lipids from different classes in OIS cells. As expected, DGAT inhibition caused a strong downregulation of almost all TG species (Fig. 4c). In contrast, the overall abundance of highly unsaturated PC, PE and O-PE lipids was increased following DGAT inhibition in OIS cells (Fig. 4d**)**. Closer inspection of individual lipid species showed that DGAT inhibition prevented the OIS-induced downregulation of PUFA-containing PC and O-PE lipids (Fig. 4e). This repartitioning of highly unsaturated acyl-chains into membrane lipids following DGAT inhibition resulted in increased ferroptosis sensitivity of OIS cells, as pre-treatment of cells with DGAT inhibitors increased sensitivity of OIS cells to RSL3 (Fig. 4f). Moreover, DGAT inhibition also resulted in a strong increase in lipid peroxidation in OIS cells exposed to RSL3 determined by Liperfluo and Bodipy$^{581/591}$ analysis (Fig. 4g, h).

Together, these results demonstrate that ferroptosis protection in OIS cells is caused by the sequestration of PUFA into TG lipids, leading to an overall reduction in highly unsaturated membrane lipids.

Ferroptosis protection is mediated by DGAT1

We next investigated whether inhibition of both DGAT enzymes is required to achieve ferroptosis sensitisation. We first queried the

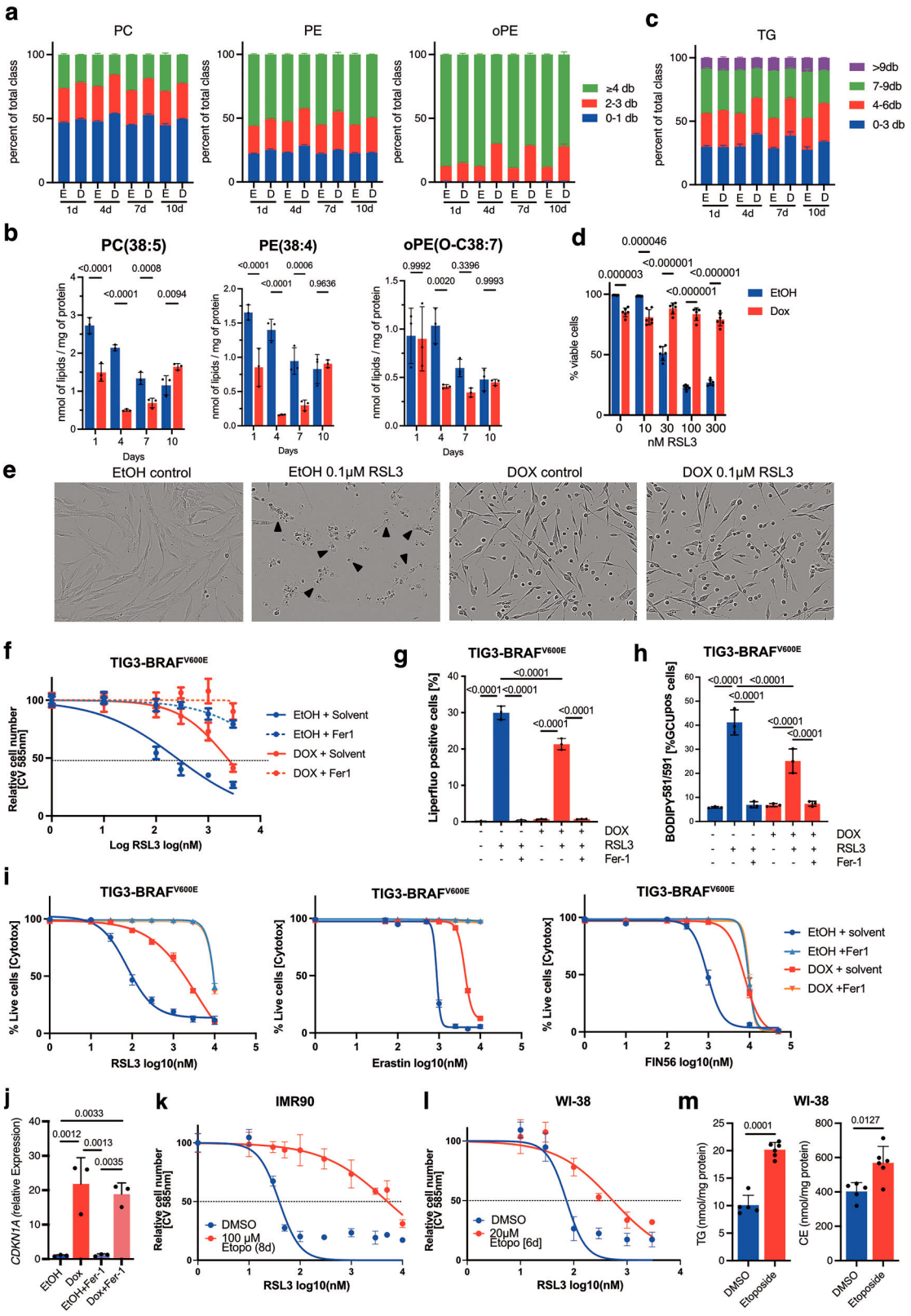

Cancer Therapeutics Response portal [46–48] to determine correlations between gene expression and drug sensitivities. Interestingly, while no association between DGAT2 expression and ferroptosis-inducing drugs was found, high expression of DGAT1 correlated with resistance towards the GPX4 inhibitors RSL3, ML210 and ML162 (Fig. 5a). We therefore applied the DGAT1 (T863) and DGAT2 (PF-06424439) inhibitors individually to TIG3 BRAF^{V600E} cells during induction of OIS. This showed that inhibition of DGAT1 was sufficient to increase ferroptosis sensitivity in OIS cells, while inhibition of DGAT2 alone had no

Fig. 3 Senescence induces remodelling of membrane lipids and resistance to ferroptosis. a Relative proportion of lipids containing fatty acids with different numbers of double bonds (db) normalised to the total amount of lipids in each class in TIG3-BRAF^{V600E} cells treated with 1 μg/ml doxycycline (DOX) or EtOH (solvent) for 1, 4, 7 or 10 days. PC = phosphatidylcholine; PE = phosphatidylethanolamine; O-PE = ether-phosphatidylethanolamine. Data represent mean ± SD of 3 independent replicates. **b** Abundance of selected PC, PE and O-PE lipids in control and OIS cells. Data represent mean ± SD ($n = 3$, two-tailed *t*-test with FDR post hoc Sidak's test). **c** Relative proportion of triglyceride (TG) lipids with different numbers of double bonds in the same samples as in **a**. **d** Viability of TIG3-BRAF^{V600E} cells treated with 1 μg/ml DOX or EtOH (solvent) for 7 days and with different concentrations of RSL3 for an additional 24 h. Viability was determined by automated cell imaging. Data represent mean ± SD of 6 independent replicates. **e** Representative images of control and 7-day OIS cells treated with 100 nM RSL3 or solvent for 24 h. Cells showing typical ferroptotic cytoplasmic swelling are indicated by arrowheads. **f** Relative cell numbers of TIG3-BRAF^{V600E} cells treated with 1 μg/ml DOX or EtOH (solvent) for 7 days and with different concentrations of RSL3 either alone or with 2 μM ferrostatin (Fer-1) for an additional 24 h. Data represent mean ± SD of 5 independent replicates. **g** Lipid peroxidation was detected using Liperfluo staining in TIG3-BRAF^{V600E} cells treated with 1 μg/ml DOX or EtOH (solvent) for 7 days and with 0.3 μM RSL3 either alone or in combination with 2 μM Fer-1 for an additional 12 h. Data represent mean ± SD ($n = 3$; significance was determined by one-way ANOVA with post hoc Tukey's test). **h** Lipid peroxidation in cells treated as in g was detected using C11-BODIPY$^{581/591}$ staining combined with live cell imaging. Data represent mean ± SD ($n = 3$; significance was determined by one-way ANOVA with post hoc Tukey's test). **i** TIG3-BRAF^{V600E} cells were treated with 1 μg/ml DOX or EtOH (solvent) for 7 days and subsequently with different concentrations of RSL3, erastin or FIN56 either alone or with 2 μM Fer-1 for an additional 24 h. Data represent mean ± SD of 5 independent replicates. **j** Expression of *CDKN1A* in TIG3-BRAF^{V600E} cells treated with 1 μg/ml DOX or EtOH (solvent) for 7 days followed by additional treatment with 2 μM Fer-1 for 48 h. Data represent mean ± SD of 3 independent replicates. Significance was calculated using one-way ANOVA with post hoc Tukey's test. **k** Relative cell numbers of IMR90 cells treated with 100 μM etoposide or solvent for 8 days and different concentrations of RSL3 for an additional 24 h ($n = 5$). **l** Relative cell number WI-38 cells treated with 20 μM etoposide or solvent for 6 days and different concentrations of RSL3 for an additional 24 h ($n = 5$). **m** Abundance of TG and CE (cholesteryl-esters) in WI-38 cells treated with 20 μM etoposide for 6 days. Data are presented as mean ± SD of 5 (DMSO) or 6 (etoposide) independent replicates. Significance was calculated using one-way ANOVA with post hoc Tukey's test.

effect (Fig. 5b). This was also corroborated by CRISPR/Cas-mediated knock-out, demonstrating that deletion of DGAT1 sensitised OIS cells to ferroptosis, while deletion of DGAT2 resulted in additional ferroptosis protection (Fig. S6a, b). A similar increase in ferroptosis sensitivity by DGAT1 inhibition was also observed in senescent WI-38 cells after etoposide treatment (Fig. S6c). However, these cells also showed elevated ferroptosis sensitivity after DGAT1 inhibition in the non-senescent state. This could be caused by the higher amounts of TG lipids found in non-senescent WI-38 cells compared to TIG3 (see Fig. 3m).

Ferroptosis is associated with morphological changes to mitochondrial size and structure [17]. We therefore investigated whether BRAF^{V600E}-induced OIS also affected mitochondrial morphology after ferroptosis induction. Consistent with previous studies [17], non-senescent TIG3 BRAF^{V600E} cells treated with 300 nM RSL3 for 6 h displayed mitochondria with reduced size and increased membrane density (Fig. 5c). We also observed individual mitochondria showing loss of cristae and membrane swelling in these cells (see detail). This phenotype was absent in OIS cells treated with the same concentration of RSL3, with their mitochondria generally displaying normal size and cristae structure. Furthermore, while DGAT1 inhibition did not alter the effect of RSL3 on mitochondrial morphology in non-senescent cells, BRAF^{V600E} OIS cells treated with the DGAT1 inhibitor also displayed reduced cristae density and evidence of mitochondrial damage (Fig. 5c). These changes in mitochondrial morphology are consistent with our conclusion that DGAT1 protects BRAF^{V600E} OIS cells from ferroptosis.

The selective function of DGAT1 and DGAT2 in ferroptosis protection could be indicative of the differential substrate specificity of these enzymes. Indeed, while DGAT2 has a higher substrate affinity, DGAT1 has been reported to have a broader substrate specificity [45]. Furthermore, DGAT1 is exclusively localised to the ER-membrane, suggesting that it could also participate in phospholipid remodelling at this site. We therefore investigated lipidomic changes in response to DGAT1 inhibition in BRAF^{V600E} OIS cells by applying untargeted lipidomic analysis, including fragmentation, to obtain more detailed insight into changes to the lipidome. Using this method, we were able to identify and quantify 343 different lipids from 19 classes, including 114 TG species (Table S5). DGAT1 inhibition also resulted in a strong reduction in TG levels (Fig. 5d), but this was less drastic than in the combined inhibition of DGAT1 and DGAT2 observed in our previous experiments (see Fig. S5a). When comparing fatty acid desaturation levels in TG lipids, we observed that DGAT1 inhibition resulted in a further increase in species containing 0-3 double bonds, representing SFA and MUFA (Fig. 5e). Conversely, membrane lipids showed a selective reduction in species containing 0-1 double bonds, representing SFA and MUFA, while species with 4 or more double bonds, representing PUFA, were increased (Fig. 5f).

Together, these data indicate that DGAT1 selectively partitions highly unsaturated fatty acids into TG lipids and reduces the availability of fatty acids for the synthesis of membrane lipids, thus increasing the ferroptosis resistance of OIS cells.

Inhibition of TG synthesis increases oxylipin production and changes the secretory phenotype of OIS cells

It has previously been shown that DGAT-dependent LD formation mediates ferroptosis suppression in slow-cycling antimitotic drug–resistant cancer cells [43]. This raised the question of whether the observed protection from ferroptosis in OIS cells is caused by TG accumulation due to cell cycle arrest. However, as we only observed a partial restoration of ferroptosis sensitivity upon DGAT1 inhibition, we wondered whether additional phenotypes that are specific to the senescent state could contribute to ferroptosis protection. It has been shown that cells induced to enter premature senescence by exposure to ionising radiation, induction of mitochondrial dysfunction or expression of HRAS^{V12} secrete large amounts of oxylipins [13]. Oxylipins are a class of lipid mediators synthesised from arachidonic acid (C20:4n-6) or dihomo-γ-linolenic acid (C20:3n-6) by the enzymatic activity of cyclooxygenases 1 and 2 (COX1 and 2) and via non-enzymatic reactions (Fig. 6a). We first confirmed that OIS induced by BRAF^{V600E} expression in TIG3 fibroblasts was accompanied by the transcriptional induction of *PTGS2*, the gene coding for COX2 (Fig. S7a). Moreover, COX2 protein levels were also strongly induced at day 7 of BRAF^{V600E} expression when cells had entered the senescent state (Fig. 6b). We therefore subjected medium from cells that had been induced to undergo OIS by 7 days of BRAF^{V600E} expression as well as controls to LC-MS analysis to selectively identify oxylipin species (Table S4). This revealed that OIS cells secrete large amounts of oxylipins, particularly several prostaglandins (PGE_2, PGA_2, PGD_1 and PGD_2) as well as 11- and 15-hydroxyeicosatetraenoic acid (11-HETE and 15-HETE) (Fig. 6c). In contrast, dihomo-15d-PGJ_2, an unusual prostaglandin shown to be a biomarker of senescence that is only released after senolysis [13], was not detected in conditioned medium from OIS cells. This

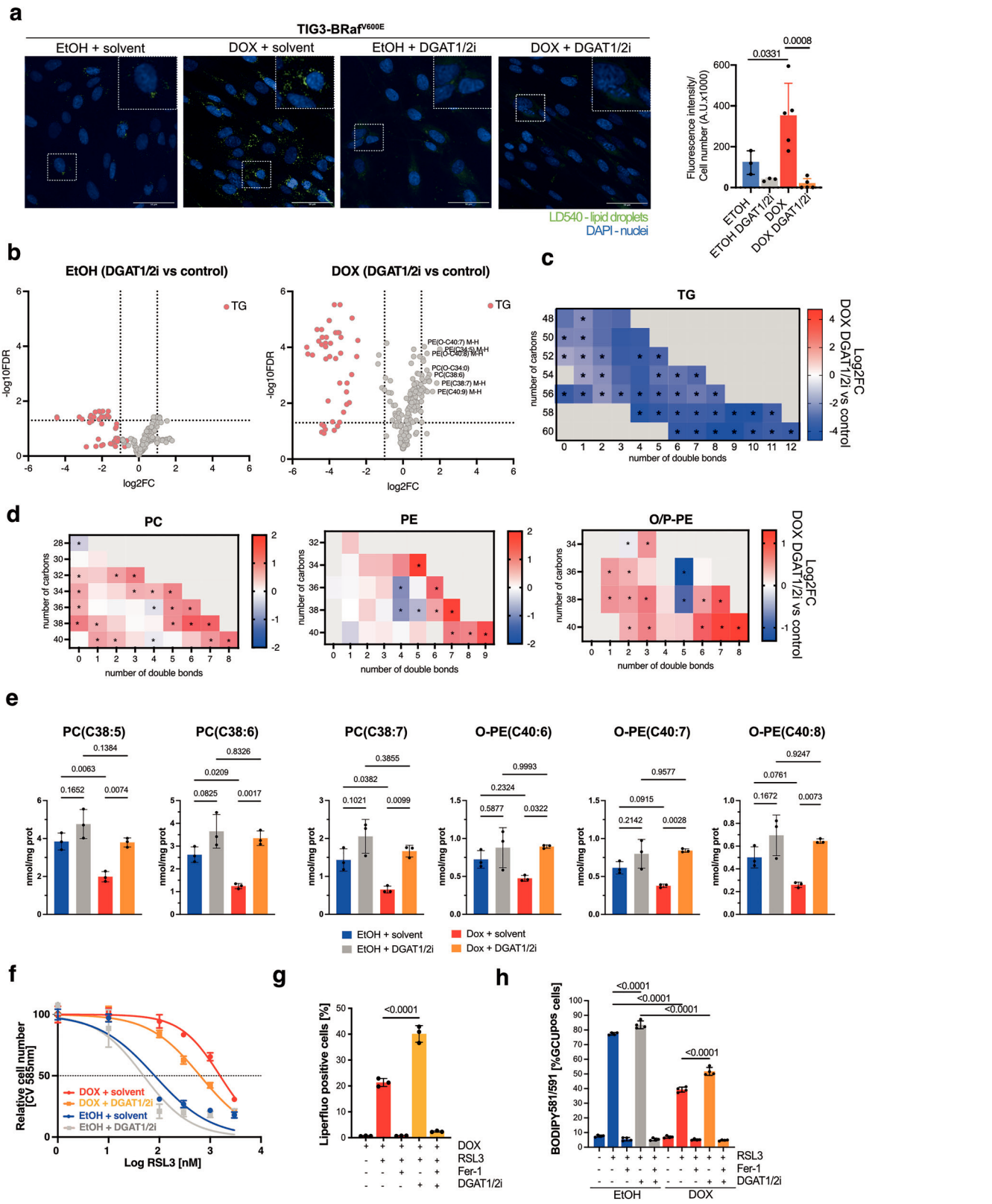

confirmed that OIS induced by BRAF^{V600E} triggers a substantial secretory phenotype involving lipid mediators.

Oxylipin production requires the availability of free *ω-6* fatty acids, facilitated by the action of phospholipases, which cleave the ester bond at the sn2 position of phospholipids. Expression of several phospholipases, including *PLA2G4A*, *PLA2G4C* and *PLA2G6*, was upregulated in BRAF^{V600E} OIS cells (Fig. S7a). As many different phospholipids carry unsaturated fatty acids in the sn2 position [14], we investigated whether OIS affects the overall abundance of different fatty acids by subjecting extracts from OIS and control cells to alkaline

Fig. 4 DGAT protects OIS cells from ferroptosis by limiting PUFA-containing phospholipids. a Lipid droplet staining of TIG3-BRAF^{V600E} cells treated 1 µg/ml doxycycline (DOX) or EtOH (solvent) either alone or in combination with 20 µM of the DGAT1 inhibitor T863 and 10 µM of the DGAT2 inhibitor PF-06424439 for 7 days. Fluorescence intensity was quantified in biologically independent replicates. Significance was calculated using one-way ANOVA with post hoc Tukey's test (ETOH $n = 3$, ETOH + DGAT1/2i $n = 3$, DOX $n = 5$, DOX + DGAT1/2i $n = 5$). **b** TIG3-BRAF^{V600E} cells were treated with 1 µg/ml DOX or EtOH (solvent) either alone or in combination with 20 µM T863 (DGAT1i) and 10 µM PF-06424439 (DGAT2i) or solvent for 7 days ($n = 3$). Volcano plot displaying lipidome changes induced by DGAT inhibition in EtOH treated cells (left) and DOX treated cells (right). Triglycerides (TG) are labelled in red. **c** Relative changes in abundance of TG species containing different numbers of carbon atoms and numbers of double bonds in OIS cells treated with 20 µM T863 and 10 µM PF-06424439 for 7 days compared to solvent controls. Data represented log2FC of normalised mean abundances. ($n = 3$; $^{*}p \leq 0.05$; unpaired two-tailed Student's *t*-test with FDR correction). **d** Relative changes in abundance of PC, PE and O/P-PE species as in **c**. **e** Abundance of selected lipid species from the same experiment as in **c**. Data represent mean ± SD ($n = 3$; significance was calculated by one-way ANOVA with post hoc Tukey's test). **f** Relative cell numbers of TIG3-BRAF^{V600E} cells treated with 1 µg/ml DOX or EtOH either alone or in combination with 20 µM T863 and 10 µM PF-06424439 for 7 days and different concentrations of RSL3 during the last 24 h. Data represent mean ± SD of 5 independent replicates. **g** Lipid peroxidation was detected by Liperfluo staining in TIG3-BRAF^{V600E} cells treated with 1 µg/ml DOX either alone or in combination with 20 µM T863 and 10 µM PF-06424439 for 7 days and 300 nM RSL3 either alone or in combination with 2 µM ferrostatin (Fer-1) during the last 12 h. Data represent mean ± SD ($n = 3$; significance was calculated by one-way ANOVA with post hoc Tukey's test). Note that samples without DGAT1/2 inhibition are also shown in Fig. 3g. **h** Lipid peroxidation was detected using C11-BODIPY$^{581/591}$ staining. TIG3-BRAF^{V600E} cells were treated with 1 µg/ml DOX either alone or in combination with 20 µM T863 and 10 µM PF-06424439 for 7 days and 300 nM RSL3 either alone or in combination with 2 µM Fer-1 followed by live cell imaging over 6 h. Data represent mean ± SD ($n = 4$; significance was calculated by one-way ANOVA with post hoc Tukey's test).

hydrolysis (saponification). Induction of BRAF^{V600E} expression resulted in a transient increase in palmitic (C16:0) and oleic acid (C18:1) (Fig. S7b). However, as FASN was not altered and expression of stearoyl-CoA desaturase (SCD) was decreased in OIS cells (Figs. S3c, d and S7c), we concluded that these fatty acids must be derived from uptake. In addition, some PUFA species, such as adrenic acid (C22:4) and docosapentaenoic acid (C22:5), showed increased abundance in OIS cells, while docosahexaenoic acid (C22:6) was decreased (Fig. S7e). While changes in these fatty acids were mostly minor, we observed a very strong reduction in the overall abundance of arachidonic acid (C20:4), with TIG3 cells after 4 days of BRAF^{V600E} OIS induction showing less than 50% compared to controls (Fig. 6d). This was accompanied by a reduction in expression of fatty acid desaturases 2 (*FADS2*), the first enzyme required for arachidonic acid synthesis, while fatty acid desaturases 1 (*FADS1*) was mostly unaffected (Fig. S7e). This suggests that in addition to the repartitioning of highly unsaturated fatty acids from membrane lipids to TG, OIS also induces an overall loss of some PUFA species, particularly arachidonic acid and docosahexaenoic acid, from the cellular lipid pool.

We next asked whether DGAT-dependent TG synthesis alters the availability of substrates for oxylipin synthesis. Combined inhibition of DGAT1 and DGAT2 during OIS induction resulted in a marked increase in the secretion of several oxylipin species, particularly PGE_2, PGA_2 and PDG_1 (Fig. 6e), without affecting the expression of *PLA2G4*, *PTGS2* and *PTGES* mRNA or COX2 protein (Figs. 6f and S7f). Consequently, the amount of arachidonic acid in the cellular lipid pool was further decreased by DGAT inhibition during OIS, although this did not reach statistical significance (Fig. 6g).

It has been shown that the production of PGE_2 and other oxylipins by senescent cells can reinforce the senescent phenotype through intracrine, autocrine and paracrine pathways [13, 49–51]. We therefore investigated whether elevated oxylipin production following DGAT inhibition could also affect the senescent phenotype of BRAF^{V600E}-expressing fibroblasts. This revealed that the expression of p21 (*CDKN1A*) and p16 (*CDKN2A*) was reduced in response to DGAT inhibition. In contrast, expression of *IL6*, a major pro-inflammatory cytokine released by senescent cells, was strongly increased following DGAT inhibition (Fig. 6h).

These results suggest that DGAT-dependent TG synthesis not only alters ferroptosis sensitivity but also modulates the secretory phenotype of OIS cells.

Inhibition of oxylipin production synergises with DGAT1 inhibition to prevent ferroptosis protection of OIS cells

We next asked whether lipidome remodelling induced by oxylipin production contributes to ferroptosis protection in OIS cells. We therefore combined inhibition of DGAT1 during OIS induction with acute treatment with the selective COX2 inhibitor celecoxib (Fig. S8a, b, and Table S5). This showed that COX2 inhibition did not alter the abundance of storage lipids (TG and CE) in OIS cells (Fig. 7a).

We next investigated the effect of COX2 and DGAT1 inhibition on the abundance of free fatty acids (FFA) in OIS cells. This showed that OIS cells strongly increase FFA abundance, particularly SFA and MUFA species, and this was reduced by individual or combined DGAT1 and COX inhibition (Fig. S8c). Levels of free linoleic acid (C18:2 n-6), arachidonic acid (C20:4 n-6) and adrenic acid (C22:4 n-6) were also elevated in OIS cells (Fig. 7b). COX2 inhibition further increased levels of free arachidonic and adrenic acids in OIS cells, most likely by blocking their conversion into oxylipins, in agreement with recent findings [13]. These results suggest that OIS cells increase the production of free arachidonic acid for oxylipin synthesis, most likely by elevating the release of these fatty acids from membrane lipids. Of note, DGAT1 inhibition reduced linoleic acid abundance but only had a minor effect on the abundance of free arachidonic acid (Fig. 7b).

To investigate whether enhanced oxylipin production in OIS cells impacts the abundance of PUFA in membrane lipids, we compared the fatty acid composition of PC, PE and plasmalogen-phosphatidylcholine (pPE) under different conditions. This showed that combined inhibition of COX2 and DGAT1 strongly increased the abundance of species containing 2-3 or more than 4 double bonds in these three lipid classes (Fig. 7c). In particular, membrane lipids containing arachidonic acid (20:4) were elevated when DGAT1 and COX2 were inhibited (Fig. 7d), suggesting that inhibition of oxylipin production increases the availability of this fatty acid for membrane lipid synthesis. This result prompted us to investigate whether combined inhibition of TG synthesis and oxylipin production could also be more efficient in increasing ferroptosis sensitivity in OIS cells. While inhibition of COX2 alone had no effect on RSL3 sensitivity, it synergised with DGAT1 inhibition in restoring ferroptosis in OIS cells to the same levels observed in non-senescent cells (IC50 = 0.2 µM) (Fig. 7e). The synergistic action of COX2 and DGAT1 was further supported by genetic deletion of *PTGS2* from TIG3-BRAF^{V600E} cells. *PTGS2* knockout cells showed elevated ferroptosis sensitivity in response to DGAT1 inhibition compared to wild-type controls during OIS (Fig. S8d). Finally, we also confirmed that addition of PGE_2 or conditioned medium from OIS cells treated with DGAT inhibitors had no effect on the ferroptosis sensitivity of non-senescent cells, excluding a paracrine effect (Fig. S8e, f).

Together, our results demonstrate that elevated TG synthesis and oxylipin production lead to global lipidome remodelling and

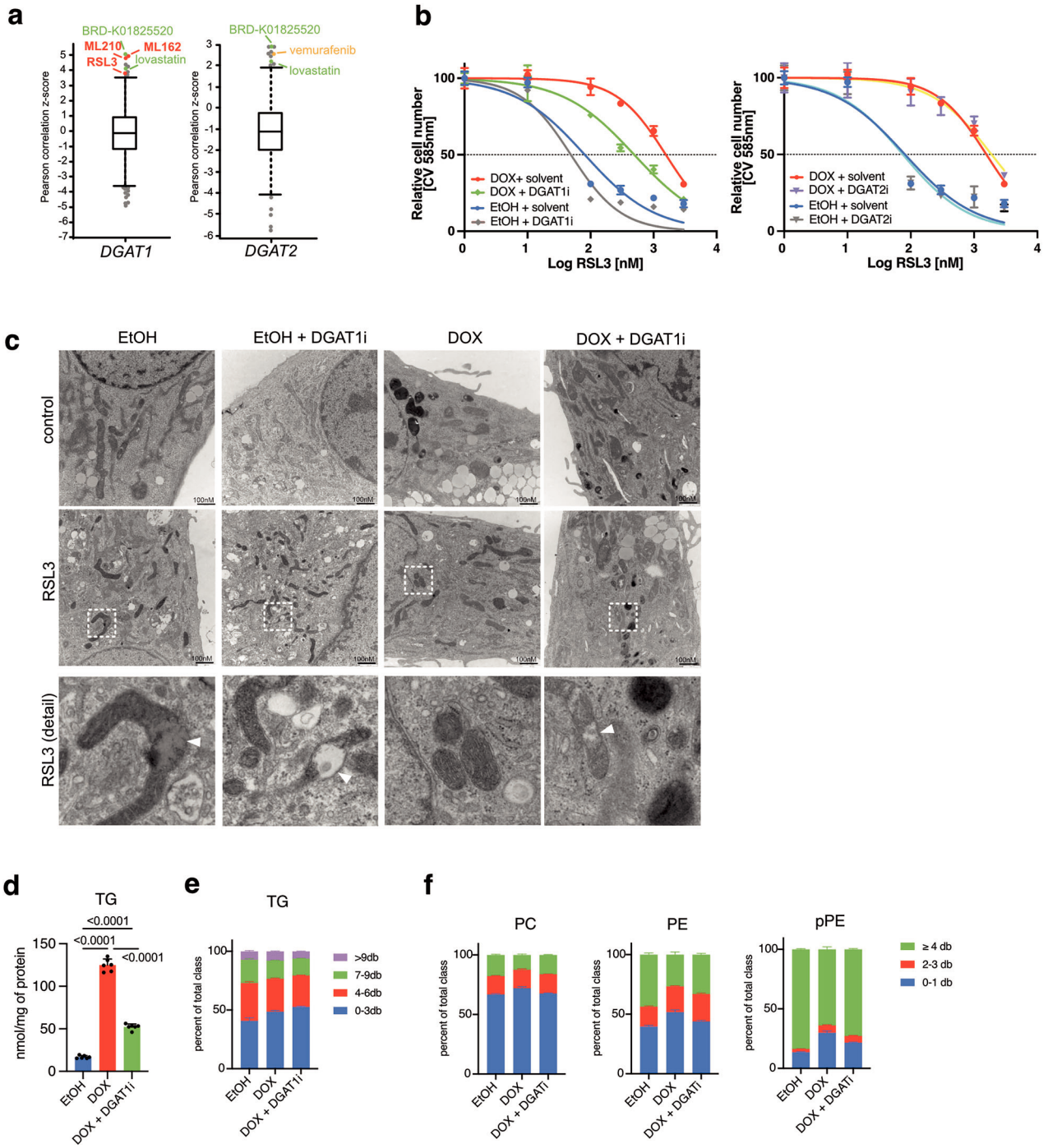

Fig. 5 Ferroptosis protection in BRAF^{V600E} OIS is mediated by DGAT1. a Box plots showing correlation between DGAT1 and DGAT2 expression and drug sensitivity for selected compounds (Cancer Therapeutics Response Portal). GPX4 inhibitors are shown in red. Plotted values are z-scored Pearson's correlation coefficients; line, median; box, 25th–75th percentile. **b** Relative cell numbers of TIG3-BRAF^{V600E} cells treated with 1 µg/ml DOX or EtOH (solvent) either alone or in combination with 20 µM of the DGAT1 inhibitor T863 (left graph) or 10 µM of the DGAT2 inhibitor PF-06424439 (right graph) for 7 days and with different concentrations of RSL3 during the last 24 h. Data represent mean ± SD of 5 independent replicates. **c** Transmission electron microscopy (TEM) analysis of TIG3-BRAF^{V600E} cells treated with 1 µg/ml DOX or EtOH (solvent) either alone or in combination with 20 µM T863 for 7 days and subsequently with 300 nM of RSL3 for 6 h. Details showing evidence of mitochondrial damage in control and DGAT1i-treated cells. **d** Abundance of TG lipids in cells TIG3-BRAF^{V600E} control and OIS cells with and without DGAT1 inhibition. **e** Relative abundance of TG lipids with different numbers of double bonds (db) in the same cells. **f** Relative abundance of PC, PE and pPE lipids with different numbers of double bonds (db).

contribute to ferroptosis resistance in OIS cells. In addition, DGAT1-dependent sequestration of PUFA into TG limits the availability of free arachidonic acid as precursors for oxylipin synthesis and shapes the secretory phenotype during OIS (Fig. 7f).

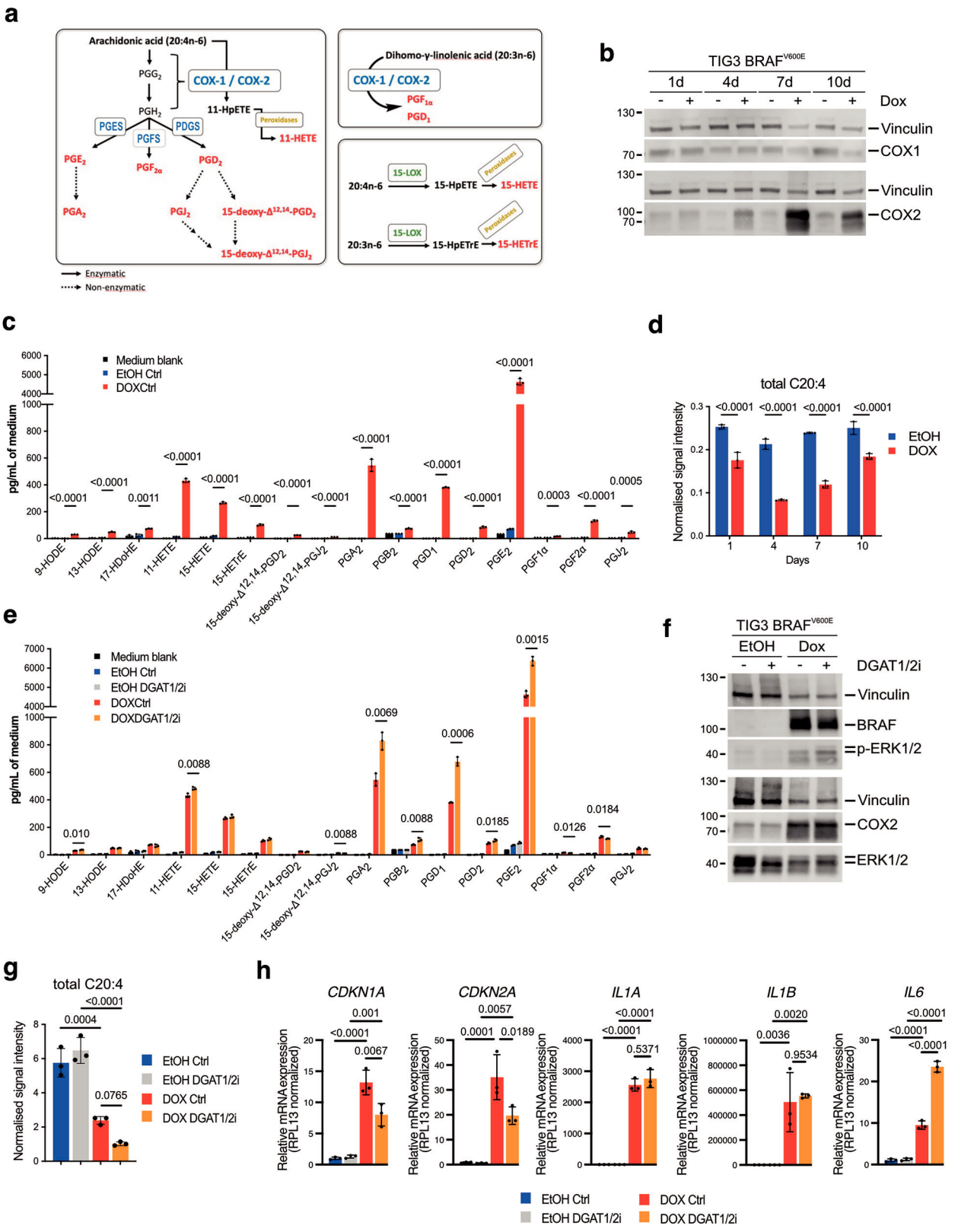

DISCUSSION

Cellular senescence is induced by different physiological and pathophysiological stress conditions, and is characterised by a stable cell cycle arrest and hyper-secretory phenotype. Senescent cells activate glucose utilisation and oxidative metabolism of pyruvate to fulfil the high bioenergetic needs of the SASP [6]. In addition, senescent cells depend on the activity of malic enzymes to counteract excess oxidative stress [52]. Lipid metabolism is intricately linked to oxidative stress, as many lipids are susceptible

Fig. 6 Inhibition of DGAT increases oxylipin production and changes the secretory phenotype of OIS cells. a Diagram showing the synthesis of different oxylipins via COX1/2, lipoxygenases (LOX) and non-enzymatic pathways. **b** WB analysis of protein lysates from TIG3-BRAF^{V600E} cells treated 1 μg/ml doxycycline (DOX) or EtOH (solvent) for 1, 4, 7 and 10 days. Vinculin is shown as loading control. Representative data from two independent experiments are shown. **c** Abundance of different oxylipins in medium collected from TIG3-BRAF^{V600E} cells treated 1 μg/ml DOX or EtOH (solvent) for 7 days. Data represented mean ± SD ($n = 3$; Significance was calculated by multiple *t*-tests with FDR correction). **d** Total abundance of arachidonic acid (C20:4) in lipids extracted by saponification from TIG3-BRAF^{V600E} cells treated 1 μg/ml DOX or EtOH (solvent) for 1, 4, 7 and 10 days. Data represented mean ± SD ($n = 3$; Significance was calculated using two-way ANOVA with post hoc Sidak's test). **e** Abundance of different oxylipins in medium collected from TIG3-BRAF^{V600E} cells treated 1 μg/ml DOX or EtOH (solvent) either alone or in combination with 20 μM of the DGAT1 inhibitor T863 and 10 μM of the DGAT2 inhibitor PF-06424439 for 7 days. Data represented mean ± SD ($n = 3$; Significance was calculated by multiple *t*-tests with FDR correction). Note that control samples are the same as in Fig. 6c. **f** WB analysis of protein lysates from TIG3-BRAF^{V600E} cells treated as in **e**. Vinculin is shown as loading control. **g** Total abundance of arachidonic acid (C20:4) in lipids extracted from TIG3-BRAF^{V600E} cells treated as in **e**. Data represented mean ± SD ($n = 3$; Significance was calculated using two-way ANOVA with post hoc Sidak's test). **h** Expression of cell cycle regulators (*CDKN1A*, *CDKN1A*) and SASP factors (*IL1A*, *IL1B* and *IL6*) in cells treated as in **e**. Data represented mean ± SD ($n = 3$; two-way ANOVA with post hoc Sidak's test). Abbreviations of molecule names: 9-hydroxyoctadecadienoic acid (9-HODE); 11-hydroxyeicosatetraenoic acid (11-HETE); 13-hydroxyoctadecadienoic acid (13-HODE); 15-hydroxyeicosatetraenoic acid (15-HETE); 15-hydroxyeicosatrienoic acid (15-HETrE); 15-hydroperoxyeicosatetraenoic acid (15-HpETE); 15-hydroperoxyeicosatrienoic acid (15-HpETrE); 17-hydroxydocosahexaenoic acid (17-HDoHE); arachidonic acid (AA); lipoxygenase 15 (15-LOX); prostaglandin A_2 (PGA_2); prostaglandin B_2 (PGB_2); prostaglandin D_1 (PGD_1); prostaglandin D_2 (PGD_2); prostaglandin E_2 (PGE_2); prostaglandin $F_{1\alpha}$ ($PGF_{1\alpha}$); prostaglandin $F_{2\alpha}$ ($PGF_{2\alpha}$); prostaglandin G_2 (PGG_2); prostaglandin H_2 (PGH_2); prostaglandin J_2 (PGJ_2).

to oxidative damage, and the accumulation of lipid peroxides triggers cell death via ferroptosis [53].

Using time-resolved transcriptomic and metabolomic analysis of human diploid fibroblasts after expression of oncogenic BRAF^{V600E}, we show here that cells undergoing OIS alter the expression of lipid metabolism genes and engage in profound remodelling of their lipidome. The most prominent changes were a marked accumulation of TG and enhanced formation of lipid droplets (LD). In addition, OIS cells induced the production of oxylipins as part of their secretory phenotype. The combined effect of enhanced TG formation and elevated oxylipin production resulted in the global remodelling of membrane phospholipids, leading to reduced PUFA abundance and ferroptosis protection. A similar accumulation of storage lipids and ferroptosis resistance was also found in human fibroblasts after induction of senescence by etoposide treatment.

Remodelling of lipid metabolism has previously been observed in different models of senescence. For example, OIS induced by ERBB2 activation has been associated with altered gene expression of lipid metabolism enzymes and specific changes in glycerophospholipids [27]. Moreover, RNAseq analysis revealed global upregulation of lipid metabolism enzymes during replicative senescence [54]. Similarly, proteomics analysis demonstrated dysregulation of lipid metabolism and accumulation of LD during therapy-induced senescence [55]. In this model, addition of TG was sufficient to induce SA-β-gal activity in fibroblasts, suggesting that aberrant lipid metabolism could also be a driver of senescence [55]. We extended these observations by demonstrating LD accumulation and colocalization with p16 in histological sections of human melanocytic naevi, confirming that increased lipid storage is associated with the senescent state also in vivo.

Mechanistically, our data show that increased TG synthesis and LD formation require the activity of DGAT enzymes. It has previously been shown that WI-38 fibroblasts exposed to different types of senescence triggers undergo a metabolic switch by activating glycerol kinase (GK) and inactivating ethanolamine-phosphate cytidylyltransferase (PCYT2) to promote TG synthesis [34]. We also observed a strong but transient upregulation of GK expression and elevated levels of glycerol-3-phosphate in BRAF^{V600E}-induced senescence. However, our stable-isotope tracing revealed that a substantial proportion of glycerol-3-phosphate is derived from glycolytic intermediates rather than exogenous glycerol, suggesting that increased glucose metabolism also contributes to TG synthesis in BRAF^{V600E}-induced OIS cells.

Previous studies investigating potential links between senescence and ferroptosis have mostly focused on iron metabolism. For example, it was shown that ferroptosis-resistant senescent fibroblasts accumulate iron due to impaired lysosomal ferritinophagy. However, restoring ferritin degradation prevented iron accumulation but failed to increase ferroptosis sensitivity [56]. A similar effect of impaired ferritinophagy was also shown in fibroblasts exposed to high-glucose [57] and in skeletal myoblasts after doxorubicin-induced senescence [58]. Furthermore, senescence-mediated iron accumulation and Gpx4 expression were found in steatotic livers of western-diet fed mice [59]. However, these studies did not provide a mechanistic explanation for the apparent ferroptosis protection in senescent cells. In addition, there is evidence linking quiescence and senescence with enhanced sensitivity towards ferroptosis [60, 61]. Interestingly, we observed that BRAF^{V600E}-induced OIS cells show protection from ferroptosis inducers targeting the SLC7A11/GSH/GPX4 axis. However, BRAF^{V600E}-OIS cells were not protected from the effect of the iron oxidant $FIN0_2$, suggesting iron-mediated lipid peroxidation is unaltered in OIS cells. As iron-mediated lipid peroxidation is initiated in the lysosome [37], and lysosomal dysfunction has been linked to ferroptosis resistance in replicative and irradiation-induced senescence [38], our findings suggest that different senescence states may induce ferroptosis resistance through distinct mechanisms.

Cell cycle arrest is generally observed in cancer cells induced to undergo quiescence or senescence in response to therapy. In this context, the quiescent therapy-resistant persister cell state has been associated with elevated sensitivity towards lipid peroxidation and ferroptosis [62]. Similarly, cell cycle arrest caused by stabilisation of p53 or by inhibition of cyclin-dependent kinases 4/6 (CDK4/6) was shown to increase ferroptosis sensitivity due to PUFA accumulation in membrane lipids [60]. It therefore seems unlikely that the ferroptosis protection observed by us in BRAF^{V600E} OIS cells is purely a consequence of cell cycle arrest. This is further supported by our finding that OIS induced by activation of oncogenic HRAS (HRAS^{V12G}) resulted in enhanced ferroptosis sensitivity. More recently, a study by Zhu and colleagues demonstrated elevated ferroptosis sensitivity as an acquired vulnerability of senescent cancer cells linked to elevated ROS induction after combined inhibition of CDK4/6 and BRD4 [61]. Together with our own findings, this demonstrates that the consequences of senescence on ferroptosis sensitivity are highly dependent on the cellular context that differs strongly between different senescence inducers and also between non-transformed and cancer cells.

Our data demonstrate that elevated TG synthesis and production of oxylipins induce global remodelling of membrane lipids that renders OIS cells resistant to ferroptosis. It has been proposed

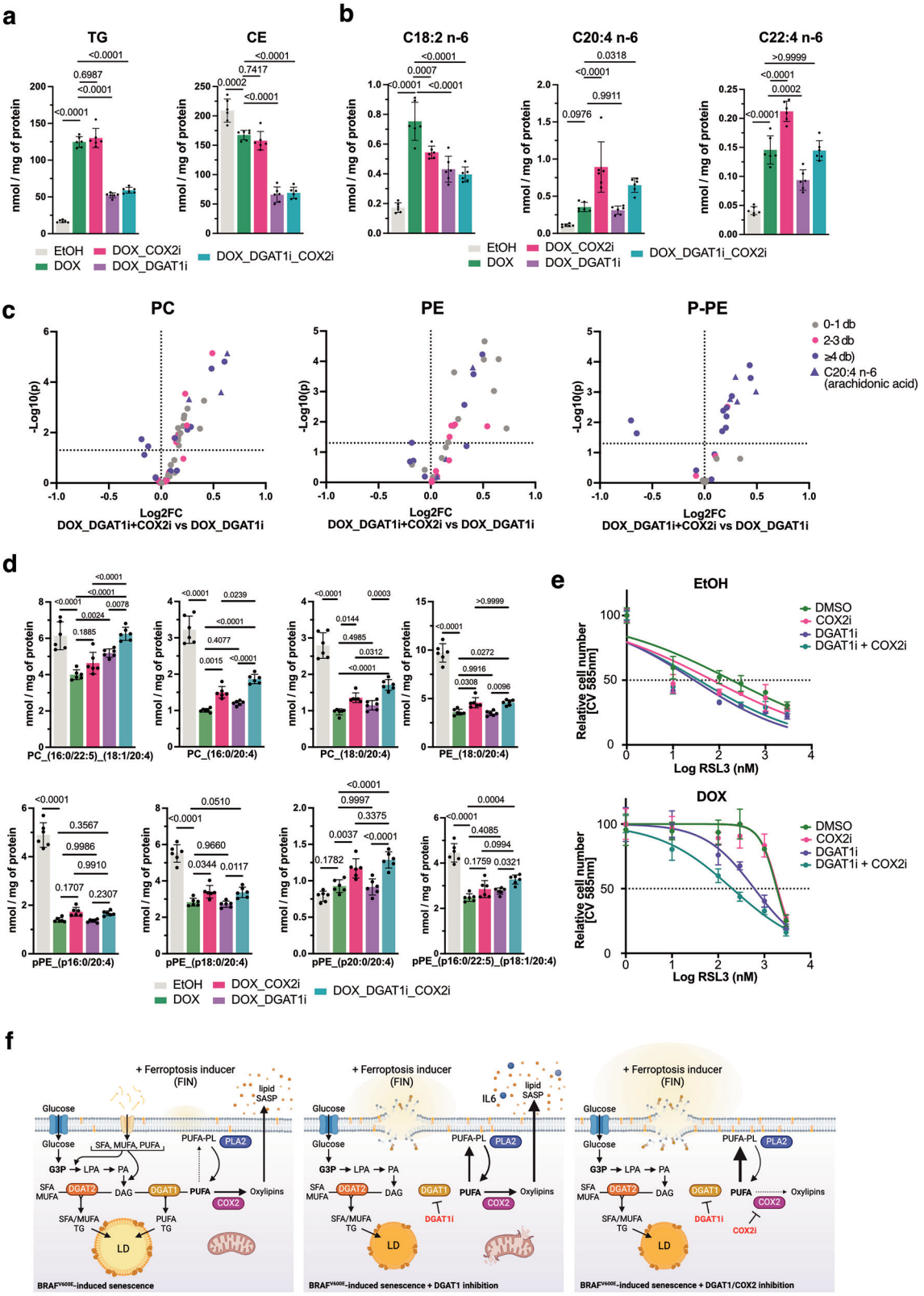

that enhanced TG synthesis protects from ferroptosis by reducing the amount of peroxidation-sensitive PUFA in membrane lipids [63]. Previously, LD formation has been shown to protect neurons from oxidative stress in the Drosophila brain [64]. Furthermore, sequestration of ω-3 and ω-6 PUFA into neutral lipids and LD was shown to mediate ferroptosis resistance in cancer cells exposed to acidic microenvironments [44]. Likewise, LD accumulation mediates ferroptosis resistance during cell cycle arrest [43]. In line with this notion, we observed that inhibition of TG synthesis by chemical blockade of DGAT1 partially restored ferroptosis

Fig. 7 Combined inhibition of DGAT1 and COX2 sensitises OIS cells to ferroptosis. a Total abundance of triglycerides (TG), cholesterol-esters (CE) in TIG3-BRAF^{V600E} cells treated with 1 μg/ml doxycycline (DOX) or EtOH (solvent) either alone or in combination with 20 μM of the DGAT1 inhibitor T863 for 7 days and with 5 μM of the selective COX2 inhibitor celecoxib for the last 24 h. Data represent mean ± SD ($n = 6$; significance was calculated by one-way ANOVA with post hoc Tukey's test). **b** Abundance of free linoleic acid (C18:2 n-6), arachidonic acid (C20:4 n-6) and adrenic acid (C22:4 n-6) in the same cells as in **a**. **c** Volcano plots displaying changes in phosphatidylcholine (PC), phosphatidylethanolamine (PE) and plasmalogen-ethanolamine (pPE) species induced by combined treatment with DGAT1 and COX2 inhibitors in OIS cells compared to inhibition of DGAT1 alone. Lipids containing only saturated and/or mono-unsaturated fatty acids (SFA + MUFA, 0-3 double bonds), poly-unsaturated fatty acids with 2-3 double bonds (2-3 db) or highly-unsaturated fatty acids containing 4 or more double bonds (≥4 db) are marked in different colours. Lipids containing arachidonic acid (20:4) are indicated by triangles. **d** Abundance of selected PC, PE and pPE lipids containing arachidonic acid (C20:4). Data represent mean ± SD ($n = 6$; significance was calculated by one-way ANOVA with post hoc Tukey's test). **e** Relative cell numbers of TIG3-BRAF^{V600E} cells treated with 1 μg/ml DOX or EtOH (solvent) either alone or in combination with 20 μM T863 for 7 days and with different concentrations of RSL3 either alone or in combination with 5 μM celecoxib for an additional 24 h ($n = 5$). **f** Model depicting the mechanism of ferroptosis protection by global lipid remodelling in BRAF^{V600E} OIS cells.

sensitivity in senescent cells by increasing the abundance of PUFA in membrane lipids. Ferroptosis protection in BRAF^{V600E} OIS cells could be mapped to the activity of DGAT1, rather than DGAT2. This was surprising, as DGAT2 showed a very strong induction in expression during OIS. Nevertheless, -our data suggest that DGAT1 selectively partitions PUFA into TG lipids, while DGAT2 seems to be responsible for incorporating SFA and MUFA. This finding is consistent with a previous study investigating the activity of ATGL and DGAT1 in hepatic stellate cells. This study suggested that different pools of TG may exist in cells: one residing in large LD with low overall turnover, mostly consisting of SFA and MUFA, and another one residing in smaller LD with higher turnover that is enriched in PUFA. DGAT1 functioning in combination with acyl-CoA synthetase 4 (ACSL4) was found to be responsible for the generation of this dynamic PUFA-containing TG pool [65]. While this hypothesis is highly attractive and consistent with our data, it should also be mentioned that inhibition of DGAT1 has also been linked to elevated oxidative stress due to deregulated fatty acid oxidation [66, 67], raising the possibility that additional mechanisms downstream of DGAT1 could contribute to ferroptosis protection.

LD also play a central role in the production of lipid mediators and can function both as sinks and sources for oxylipin precursors [68]. Importantly, the production of oxylipins is part of the hypersecretory phenotype of senescent cells [13]. We found that BRAF^{V600E} OIS cells showed upregulation of several PLA_2 isoforms, as well as elevated expression of COX2. We also observed a strong induction in the secretion of multiple oxylipins, particularly PGE_2, PGA_2, PGD_1, 11-HETE and 15-HETE. We also observed a large drop in the total abundance of arachidonic acid, the substrate of the majority of oxylipins secreted by OIS cells. The scale of this effect was surprising, given that oxylipins are produced in minute amounts by most cell types [69]. However, our results suggest that the strong induction of oxylipin production in senescent cells could represent a major drain on the arachidonic acid pool, resulting in reduced availability of this fatty acid for the synthesis of membrane lipids. Consequently, COX2 inhibition increased the abundance of arachidonic acid and other highly unsaturated fatty acids in membrane phospholipids. Interestingly, the effect of OIS on arachidonic acid levels was transient, peaking at 4–7 days of BRAF^{V600E} induction, in line with the transient induction of COX2 protein. This was also mirrored by the increase in PUFA-containing oPE lipids observed after 10 days of OIS induction. This suggests that the acute induction of inflammation during the early stages of OIS has specific effects on lipid composition.

Activation of PUFA for subsequent lipid synthesis requires the activity of ACSL4, an enzyme that is well known to promote ferroptosis [70, 71]. Our findings suggest that COX2 competes with ACSL4 for the same pool of arachidonic acid. Indeed, it has previously been shown that overexpression of ACSL4 blunts PGE_2 secretion by vascular smooth muscle cells [72]. However, long-term inhibition of ACSL4 reduced PGE_2 production, presumably by lowering the abundance of arachidonic acid in membrane lipids. Our results also indicate that DGAT1 and COX2 act synergistically to protect senescent cells from ferroptosis, as the effect of COX2 inhibition was only observed when TG synthesis was also blocked. One possible explanation for this could be that TG act as a reservoir for arachidonic acid and other PUFA, as previously suggested [73]. Sequestration to LD reduces the availability of these fatty acids for the production of oxylipins and for their incorporation into phospholipids. Indeed, we found that combined inhibition of DGAT1 and COX2 increased the abundance of free arachidonic and adrenic acid in OIS cells. Furthermore, the abundance of arachidonic acid in membrane lipids was increased after combined inhibition of DGAT1 and COX2 compared to the effect of COX2 inhibition alone. Inhibition of DGAT also increased oxylipin secretion by OIS cells, suggesting that TG synthesis limits the availability of substrates for this process. This was accompanied by increased induction of *IL6*, confirming that TG synthesis modulates both the protein and the lipid SASP.

Our study raises interesting questions linked to the interplay between lipid metabolism and oxidative stress resistance in cancer and other diseases. It was recently shown that inhibition of DGAT1 blocks the proliferation of human melanoma cells and its deletion prevented tumour formation in a BRAF^{V600E}-dependent zebrafish model [74]. Furthermore, inhibition of DGAT1 induced lipotoxicity in melanoma cells and rendered them highly sensitive to oxidative stress [66]. Thus, the mechanisms that protect vulnerable lipids from oxidative damage during senescence could be maintained after cells have undergone senescence bypass or senescence escape and contribute to oxidative stress resistance in cancer. Furthermore, altered lipid metabolism associated with obesity and metabolic syndrome could mediate ferroptosis protection in pre-cancerous cells. Likewise, DGAT1-dependent LD formation could also affect the accumulation of senescent cells in ageing tissues. Elucidating the role of DGAT1 and COX2 in lipid metabolism and oxidative stress resistance could thus provide insight into diverse pathologies.

DATA AVAILABILITY

Raw data is provided in supplemental tables. Any additional information is available from the lead contact upon request.

REFERENCES

1. Schmitt CA, Wang B, Demaria M. Senescence and cancer - role and therapeutic opportunities. Nat Rev Clin Oncol. 2022;19:619–36.
2. Kang TW, Yevsa T, Woller N, Hoenicke L, Wuestefeld T, Dauch D, et al. Senescence surveillance of pre-malignant hepatocytes limits liver cancer development. Nature. 2011;479:547–51.
3. Eggert T, Wolter K, Ji J, Ma C, Yevsa T, Klotz S, et al. Distinct functions of senescence-associated immune responses in liver tumor surveillance and tumor progression. Cancer Cell. 2016;30:533–47.

4. Pereira BI, Devine OP, Vukmanovic-Stejic M, Chambers ES, Subramanian P, Patel N, et al. Senescent cells evade immune clearance via HLA-E-mediated NK and CD8(+) T cell inhibition. Nat Commun. 2019;10:2387.
5. Milanovic M, Fan DNY, Belenki D, Dabritz JHM, Zhao Z, Yu Y, et al. Senescence-associated reprogramming promotes cancer stemness. Nature. 2018;553:96–100.
6. Wiley CD, Campisi J. From ancient pathways to aging cells-connecting metabolism and cellular senescence. Cell Metab. 2016;23:1013–21.
7. Aird KM, Zhang G, Li H, Tu Z, Bitler BG, Garipov A, et al. Suppression of nucleotide metabolism underlies the establishment and maintenance of oncogene-induced senescence. Cell Rep. 2013;3:1252–65.
8. Kaplon J, Zheng L, Meissl K, Chaneton B, Selivanov VA, Mackay G, et al. A key role for mitochondrial gatekeeper pyruvate dehydrogenase in oncogene-induced senescence. Nature. 2013;498:109–12.
9. Dorr JR, Yu Y, Milanovic M, Beuster G, Zasada C, Dabritz JH, et al. Synthetic lethal metabolic targeting of cellular senescence in cancer therapy. Nature. 2013;501:421–5.
10. Quijano C, Cao L, Fergusson MM, Romero H, Liu J, Gutkind S, et al. Oncogene-induced senescence results in marked metabolic and bioenergetic alterations. Cell Cycle. 2012;11:1383–92.
11. Pluquet O, Pourtier A, Abbadie C. The unfolded protein response and cellular senescence. A review in the theme: cellular mechanisms of endoplasmic reticulum stress signaling in health and disease. Am J Physiol Cell Physiol. 2015;308:C415–25.
12. Wiley CD, Velarde MC, Lecot P, Liu S, Sarnoski EA, Freund A, et al. Mitochondrial dysfunction induces senescence with a distinct secretory phenotype. Cell Metab. 2016;23:303–14.
13. Wiley CD, Sharma R, Davis SS, Lopez-Dominguez JA, Mitchell KP, Wiley S, et al. Oxylipin biosynthesis reinforces cellular senescence and allows detection of senolysis. Cell Metab. 2021;33:1124–36.e5.
14. Park JB, Lee CS, Jang JH, Ghim J, Kim YJ, You S, et al. Phospholipase signalling networks in cancer. Nat. Rev. Cancer. 2012;12:782–92.
15. Kim HJ, Kim KS, Kim SH, Baek SH, Kim HY, Lee C, et al. Induction of cellular senescence by secretory phospholipase A2 in human dermal fibroblasts through an ROS-mediated p53 pathway. J Gerontol A Biol. Sci. Med. Sci. 2009;64:351–62.
16. Ai Y, Meng Y, Yan B, Zhou Q, Wang X. The biochemical pathways of apoptotic, necroptotic, pyroptotic, and ferroptotic cell death. Mol. Cell. 2024;84:170–9.
17. Dixon SJ, Lemberg KM, Lamprecht MR, Skouta R, Zaitsev EM, Gleason CE, et al. Ferroptosis: an iron-dependent form of nonapoptotic cell death. Cell. 2012;149:1060–72.
18. Conrad M, Pratt DA. The chemical basis of ferroptosis. Nat. Chem. Biol. 2019;15:1137–47.
19. Friedmann Angeli JP, Miyamoto S, Schulze A. Ferroptosis: the greasy side of cell death. Chem. Res. Toxicol. 2019;32:362–9.
20. Kim JH, Choi HS, Kim SL, Lee DS. The PAK1-Stat3 signaling pathway activates IL-6 gene transcription and human breast cancer stem cell formation. Cancers. 2019;11:1527.
21. Koundouros N, Karali E, Tripp A, Valle A, Inglese P, Perry NJS, et al. Metabolic fingerprinting links oncogenic PIK3CA with enhanced arachidonic acid-derived eicosanoids. Cell. 2020;181:1596–611.e27.
22. Geiger TR, Song JY, Rosado A, Peeper DS. Functional characterization of human cancer-derived TRKB mutations. PLoS ONE. 2011;6:e16871.
23. Dimri GP, Lee X, Basile G, Acosta M, Scott G, Roskelley C, et al. A biomarker that identifies senescent human cells in culture and in aging skin in vivo. Proc Natl Acad Sci. USA. 1995;92:9363–7.
24. Narita M, Nunez S, Heard E, Narita M, Lin AW, Hearn SA, et al. Rb-mediated heterochromatin formation and silencing of E2F target genes during cellular senescence. Cell. 2003;113:703–16.
25. Bligh EG, Dyer WJ. A rapid method of total lipid extraction and purification. Can J Biochem Physiol. 1959;37:911–7.
26. Chaves-Filho AB, Diniz LS, Santos RS, Lima RS, Oreliana H, Pinto IFD, et al. Plasma oxylipin profiling by high resolution mass spectrometry reveal signatures of inflammation and hypermetabolism in amyotrophic lateral sclerosis. Free Radic Biol. Med. 2023;208:285–98.
27. Cadenas C, Vosbeck S, Hein EM, Hellwig B, Langer A, Hayen H, et al. Glycerophospholipid profile in oncogene-induced senescence. Biochim. Biophys. Acta. 2012;1821:1256–68.
28. Olzmann JA, Carvalho P. Dynamics and functions of lipid droplets. Nat. Rev. Mol. Cell Biol. 2019;20:137–55.
29. Spandl J, White DJ, Peychl J, Thiele C. Live cell multicolor imaging of lipid droplets with a new dye, LD540. Traffic. 2009;10:1579–84.
30. Hodis E, Torlai Triglia E, Kwon JYH, Biancalani T, Zakka LR, Parkar S, et al. Stepwise-edited, human melanoma models reveal mutations' effect on tumor and microenvironment. Science. 2022;376:eabi8175.
31. Lee AH, Scapa EF, Cohen DE, Glimcher LH. Regulation of hepatic lipogenesis by the transcription factor XBP1. Science. 2008;320:1492–6.
32. Blazanin N, Son J, Craig-Lucas AB, John CL, Breech KJ, Podolsky MA, et al. ER stress and distinct outputs of the IRE1alpha RNase control proliferation and senescence in response to oncogenic Ras. Proc. Natl. Acad Sci. USA. 2017;114:9900–5.
33. Igelmann S, Lessard F, Uchenunu O, Bouchard J, Fernandez-Ruiz A, Rowell MC, et al. A hydride transfer complex reprograms NAD metabolism and bypasses senescence. Mol Cell. 2021;81:3848–65 e19.
34. Tighanimine K, Nabuco Leva Ferreira Freitas JA, Nemazanyy I, Bankole A, Benarroch-Popivker D, Brodesser S, et al. A homoeostatic switch causing glycerol-3-phosphate and phosphoethanolamine accumulation triggers senescence by rewiring lipid metabolism. Nat. Metab. 2024;6:323–42.
35. Berndt C, Alborzinia H, Amen VS, Ayton S, Barayeu U, Bartelt A, et al. Ferroptosis in health and disease. Redox Biol. 2024;75:103211.
36. Stockwell BR. Ferroptosis turns 10: emerging mechanisms, physiological functions, and therapeutic applications. Cell. 2022;185:2401–21.
37. Cañeque T, Baron L, Müller S, Carmona A, Colombeau L, Versini A, et al. Activation of lysosomal iron triggers ferroptosis in cancer. Nature. 2025;642:492–500.
38. Loo TM, Zhou X, Tanaka Y, Sugawara S, Yamauchi S, Kawasaki H, et al. Senescence-associated lysosomal dysfunction impairs cystine deprivation-induced lipid peroxidation and ferroptosis. Nat. Commun. 2025;16:6617.
39. Chien Y, Scuoppo C, Wang X, Fang X, Balgley B, Bolden JE, et al. Control of the senescence-associated secretory phenotype by NF-kappaB promotes senescence and enhances chemosensitivity. Genes. Dev. 2011;25:2125–36.
40. Contrepois K, Coudereau C, Benayoun BA, Schuler N, Roux PF, Bischof O, et al. Histone variant H2A.J accumulates in senescent cells and promotes inflammatory gene expression. Nat. Commun. 2017;8:14995.
41. Dolma S, Lessnick SL, Hahn WC, Stockwell BR. Identification of genotype-selective antitumor agents using synthetic lethal chemical screening in engineered human tumor cells. Cancer Cell. 2003;3:285–96.
42. Yang WS, Stockwell BR. Synthetic lethal screening identifies compounds activating iron-dependent, nonapoptotic cell death in oncogenic-RAS-harboring cancer cells. Chem. Biol. 2008;15:234–45.
43. Lee H, Horbath A, Kondiparthi L, Meena JK, Lei G, Dasgupta S, et al. Cell cycle arrest induces lipid droplet formation and confers ferroptosis resistance. Nat. Commun. 2024;15:79.
44. Dierge E, Debock E, Guilbaud C, Corbet C, Mignolet E, Mignard L, et al. Peroxidation of n-3 and n-6 polyunsaturated fatty acids in the acidic tumor environment leads to ferroptosis-mediated anticancer effects. Cell Metab. 2021;33:1701–15 e5.
45. Yen CL, Stone SJ, Koliwad S, Harris C, Farese RV Jr. Thematic review series: glycerolipids. DGAT enzymes and triacylglycerol biosynthesis. J Lipid Res. 2008;49:2283–301.
46. Basu A, Bodycombe NE, Cheah JH, Price EV, Liu K, Schaefer GI, et al. An interactive resource to identify cancer genetic and lineage dependencies targeted by small molecules. Cell. 2013;154:1151–61.
47. Seashore-Ludlow B, Rees MG, Cheah JH, Cokol M, Price EV, Coletti ME, et al. Harnessing connectivity in a large-scale small-molecule sensitivity dataset. Cancer Discov. 2015;5:1210–23.
48. Rees MG, Seashore-Ludlow B, Cheah JH, Adams DJ, Price EV, Gill S, et al. Correlating chemical sensitivity and basal gene expression reveals mechanism of action. Nat. Chem. Biol. 2016;12:109–16.
49. Martien S, Pluquet O, Vercamer C, Malaquin N, Martin N, Gosselin K, et al. Cellular senescence involves an intracrine prostaglandin E2 pathway in human fibroblasts. Biochim. Biophys. Acta. 2013;1831:1217–27.
50. Dagouassat M, Gagliolo JM, Chrusciel S, Bourin MC, Duprez C, Caramelle P, et al. The cyclooxygenase-2-prostaglandin E2 pathway maintains senescence of chronic obstructive pulmonary disease fibroblasts. Am J Respir Crit Care Med. 2013;187:703–14.
51. Kabir TD, Leigh RJ, Tasena H, Mellone M, Coletta RD, Parkinson EK, et al. A miR-335/COX-2/PTEN axis regulates the secretory phenotype of senescent cancer-associated fibroblasts. Aging. 2016;8:1608–35.
52. Jiang P, Du W, Mancuso A, Wellen KE, Yang X. Reciprocal regulation of p53 and malic enzymes modulates metabolism and senescence. Nature. 2013;493:689–93.
53. Li Z, Lange M, Dixon SJ, Olzmann JA. Lipid quality control and ferroptosis: from concept to mechanism. Annu Rev Biochem. 2023;93:499–528.
54. Saitou M, Lizardo DY, Taskent RO, Millner A, Gokcumen O, Atilla-Gokcumen GE. An evolutionary transcriptomics approach links CD36 to membrane remodeling in replicative senescence. Mol Omics. 2018;14:237–46.
55. Flor AC, Wolfgeher D, Wu D, Kron SJ. A signature of enhanced lipid metabolism, lipid peroxidation and aldehyde stress in therapy-induced senescence. Cell Death Discov. 2017;3:17075.
56. Masaldan S, Clatworthy SAS, Gamell C, Meggyesy PM, Rigopoulos AT, Haupt S, et al. Iron accumulation in senescent cells is coupled with impaired ferritinophagy and inhibition of ferroptosis. Redox Biol. 2018;14:100–15.

57. Wei X, Liu M, Zheng Z, Yu S, Huang L, Ma J, et al. Defective NCOA4-dependent ferroptosis in senescent fibroblasts retards diabetic wound healing. Cell Death Discov. 2023;9:138.
58. Feng Y, Wei H, Lyu M, Yu Z, Chen J, Lyu X, et al. Iron retardation in lysosomes protects senescent cells from ferroptosis. Aging. 2024;16:7683–703.
59. Vetuschi A, Cappariello A, Onori P, Gaudio E, Latella G, Pompili S, et al. Ferroptosis resistance cooperates with cellular senescence in the overt stage of nonalcoholic fatty liver disease/nonalcoholic steatohepatitis. Eur J Histochem. 2022;66:3391.
60. Rodencal J, Kim N, He A, Li VL, Lange M, He J, et al. Sensitization of cancer cells to ferroptosis coincident with cell cycle arrest. Cell Chem. Biol. 2023;31:234–48.e13.
61. Zhu X, Fu Z, Dutchak K, Arabzadeh A, Milette S, Steinberger J, et al. Cotargeting CDK4/6 and BRD4 promotes senescence and ferroptosis sensitivity in cancer. Cancer Res. 2024;84:1333–51.
62. Hangauer MJ, Viswanathan VS, Ryan MJ, Bole D, Eaton JK, Matov A, et al. Drug-tolerant persister cancer cells are vulnerable to GPX4 inhibition. Nature. 2017;551:247–50.
63. Danielli M, Perne L, Jarc Jovicic E, Petan T. Lipid droplets and polyunsaturated fatty acid trafficking: balancing life and death. Front Cell Dev. Biol. 2023;11:1104725.
64. Bailey AP, Koster G, Guillermier C, Hirst EM, MacRae JI, Lechene CP, et al. Antioxidant role for lipid droplets in a stem cell niche of Drosophila. Cell. 2015;163:340–53.
65. Tuohetahuntila M, Molenaar MR, Spee B, Brouwers JF, Houweling M, Vaandrager AB, et al. ATGL and DGAT1 are involved in the turnover of newly synthesized triacylglycerols in hepatic stellate cells. J Lipid Res. 2016;57:1162–74.
66. Wilcock DJ, Badrock AP, Wong CW, Owen R, Guerin M, Southam AD, et al. Oxidative stress from DGAT1 oncoprotein inhibition in melanoma suppresses tumor growth when ROS defenses are also breached. Cell Rep. 2022;39:110995.
67. Cheng X, Geng F, Pan M, Wu X, Zhong Y, Wang C, et al. Targeting DGAT1 ameliorates glioblastoma by increasing fat catabolism and oxidative stress. Cell Metab. 2020;32:229–42 e8.
68. Jarc E, Petan T. A twist of FATe: lipid droplets and inflammatory lipid mediators. Biochimie. 2020;169:69–87.
69. Wang D, Dubois RN. Eicosanoids and cancer. Nat Rev Cancer. 2010;10:181–93.
70. Kagan VE, Mao G, Qu F, Angeli JP, Doll S, Croix CS, et al. Oxidized arachidonic and adrenic PEs navigate cells to ferroptosis. Nat. Chem. Biol. 2017;13:81–90.
71. Doll S, Proneth B, Tyurina YY, Panzilius E, Kobayashi S, Ingold I, et al. ACSL4 dictates ferroptosis sensitivity by shaping cellular lipid composition. Nat. Chem. Biol. 2017;13:91–8.
72. Golej DL, Askari B, Kramer F, Barnhart S, Vivekanandan-Giri A, Pennathur S, et al. Long-chain acyl-CoA synthetase 4 modulates prostaglandin E(2) release from human arterial smooth muscle cells. J Lipid Res. 2011;52:782–93.
73. Petan T. Lipid droplets in cancer. Rev Physiol Biochem. Pharmacol. 2023;185:53–86.
74. Lumaquin-Yin D, Montal E, Johns E, Baggiolini A, Huang TH, Ma Y, et al. Lipid droplets are a metabolic vulnerability in melanoma. Nat. Commun. 2023;14:3192.

ACKNOWLEDGEMENTS

The authors wish to thank K. Richter (Core Facility Electron Microscopy, DKFZ Heidelberg) for expert support. The authors also acknowledge I. Germer and S. Haid for technical assistance and all members of the Schulze lab for helpful discussions. Tissue samples were processed by the tissue bank of the University Medical Center Mainz in accordance with the regulations of the tissue biobank and the approval of the ethics committee of University Medical Center Mainz.

AUTHOR CONTRIBUTIONS

MSH, MTS and AS conceived the study; MSH, KMA-S, CDC, JH, FCEV, DG, IK and MCA conducted experiments; LS and ABCF performed metabolomics and lipidomic analyses; SW, CA and PP performed RNAseq and data analysis; BS performed histological staining; JSU provided tissue samples; SM, ME and MTR provided essential resources and insight. MSH, KMA-S and AS wrote the manuscript with critical input from all authors.

FUNDING INFORMATION

AS discloses support for this work from the German Research Foundation (SCHU2670/2-2, SCHU2670/3-2 and SCHM1622/11-1) and the German Ministry of Science and Education (SMART-NAFLD). K.A.-S. acknowledges a personal fellowship by the German Academic Exchange Service (DAAD). ABC-F was funded by a fellowship from Fundação de Amparo à Pesquisa do Estado de São Paulo (FAPESP 2021/10153-5). Open Access funding enabled and organized by Projekt DEAL.

COMPETING INTERESTS

The authors declare no competing interests.

ADDITIONAL INFORMATION

Supplementary information The online version contains supplementary material available at https://doi.org/10.1038/s41418-026-01766-x.

Correspondence and requests for materials should be addressed to Almut Schulze.

Reprints and permission information is available at http://www.nature.com/reprints

Publisher's note Springer Nature remains neutral with regard to jurisdictional claims in published maps and institutional affiliations.